
Inference-Time Search Using Side Information for Diffusion-Based Image Reconstruction

Mahdi Farahbakhsh^{*†} Vishnu Teja Kunde^{*†}

Dileep Kalathil[†] Krishna Narayanan[†] Jean-Francois Chamberland[†]

Abstract

Diffusion models have been used as priors for solving inverse problems. However, existing approaches typically overlook side information that could significantly improve reconstruction quality, especially in severely ill-posed settings. In this work, we propose a novel framework that incorporates side information into existing diffusion-based inverse problem solvers via inference-time search, in a plug-and-play, training-free manner. Through extensive experiments across a range of inverse problems, including inpainting, super-resolution, and several deblurring tasks, and across multiple diffusion-based inverse problem solvers (DPS, DAPS, and MPGD), we show that augmenting each solver with our framework consistently improves the quality of the reconstructions over the corresponding original method. To demonstrate the generality of our approach, we consider diverse forms of side information, including reference images, textual descriptions, and anatomical MRI scans. The code is available at this repository³.

1 Introduction

Diffusion models [Ho et al., 2020, Song et al., 2021b] have shown remarkable success in diverse generative tasks like text-to-image synthesis [Rombach et al., 2022], protein generation [Wu et al., 2024], video [Ho et al., 2022], audio [Kong et al., 2021], and language modeling [Sahoo et al., 2024]. Beyond generation, these models have shown great promise in **solving inverse problems**, where the goal is to reconstruct an image from partial or noisy observations [Chung et al., 2023b, Daras et al., 2024]. A key distinction is that unlike many generative tasks (e.g., text-to-image synthesis, personalized editing, style transfer), which are often judged subjectively, inverse problems have a precise objective: to recover the ground-truth signal from incomplete measurements.

When the observation is heavily degraded, the inverse problem becomes highly ill-posed as many reconstructions can explain the measurements almost equally well. In this regime, unconstrained posterior sampling rarely recovers the ground truth. A practical solution is to incorporate **side information**, defined as auxiliary measurements perceptually related to the target signal, to constrain the solution space and guide reconstruction. This idea is well established in classical signal processing, where structural or encoded properties are used to guide the iterative algorithms that solve the inverse problem [Jones, 2009, Chun et al., 2012, Oymak et al., 2013, Ehrhardt et al., 2014, Mota et al., 2017, Hyder et al., 2019]. In medical imaging, complementary measurements or modalities, such as multiple MRI contrasts, multimodal microscopy, or RGB guidance for NIR imaging, have been shown to substantially improve quality [Atalık et al., 2025, Tsiligianni and Deligiannis, 2019].

^{*}Equal Contribution.

[†]Department of Electrical and Computer Engineering, Texas A&M University, College Station, TX-77843. {mahdi.farahbakhsh, vishnukunde, dileep.kalathil, krn, chmbrlnd}@tamu.edu

³<https://github.com/mahdi-farahbakhsh/DISS>

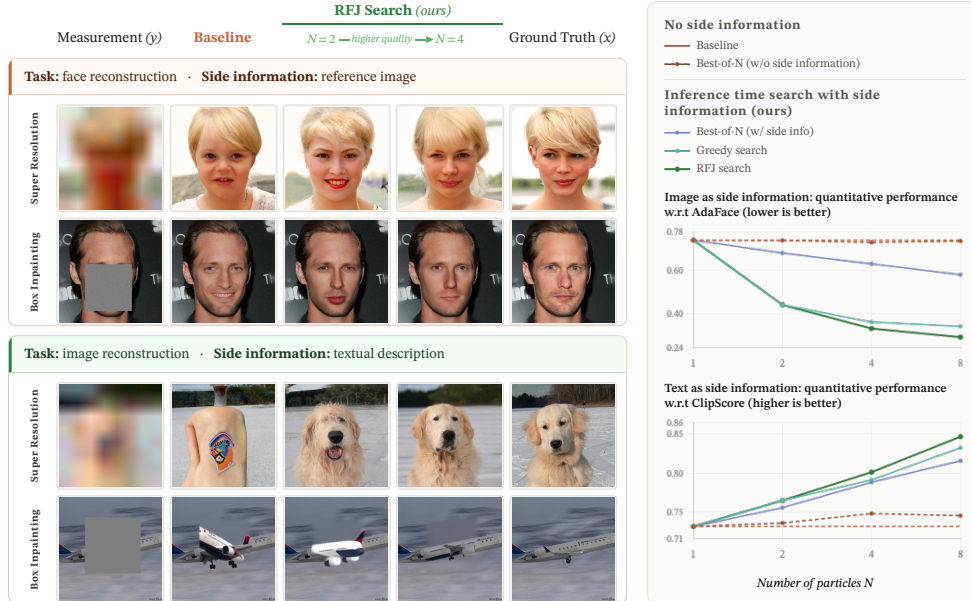


Figure 1: Incorporating side information via inference-time search improves reconstructions. (Left) Our framework augments state-of-the-art inverse problem solvers [Chung et al., 2023b,a, Zhang et al., 2025, He et al., 2024] with side information through inference-time search, yielding perceptually superior reconstructions with quality further improving as the number of particles N increases. (Right) All search algorithms within our side-information framework scale significantly better with additional compute than baselines without side information, demonstrating our framework’s effectiveness.

While the existing works on diffusion-based solvers have made significant progress on inverse problems, they largely sidestep the harder and increasingly common setting where we must also exploit side information (e.g., a reference photograph of the same person, a text description, or features from another modality). A key obstacle is the challenge of learning the conditional distribution $p_{X|Y,S}$, where X denotes the target image, Y denotes the noisy measurement, and S denotes the side information. While some recent works [Kim et al., 2025a, Chung et al., 2025] address the limited setting of textual side information, these approaches typically train a diffusion model to take a specific side information modality as input; this demands large paired datasets and expensive training, ties the solver to a single conditioning format, and is impractical when the test-time side information differs from what the model was trained on. This motivates us to address the following question:

How can we leverage a pre-trained (unconditional) diffusion prior to solve inverse problems with side information at inference time, without any retraining, so that the method is modality-agnostic and can use text, images, or features depending on the end-use applications? We provide constructive solutions to these questions in our work. Our main contributions are the following.

- **Modeling:** We introduce an approach that incorporates arbitrary side information via an auxiliary reward, characterizing the posterior $p_{X|S}$ as a reward-tilted version of the pre-trained diffusion prior. This abstraction decouples the measurement model from the side information, is modality-agnostic (text, image, features), and requires no retraining. We derive tractable approximations with error bounds for the conditional score functions needed for sampling from pre-trained diffusion models.
- **Algorithm:** Motivated by inference-time search successes in LLMs [Snell et al., 2025, Setlur et al., 2025, Liu et al., 2025], we incorporate side information via inference time search. We use an off-the-shelf reward function scoring reconstructions by consistency with the side information. We consider two search strategies: Greedy Search (GS), an SMC-based approach that periodically selects the highest reward particles, and Recursive Fork-Join Search (RFJS), which resamples within dynamic particle groups, preserving diversity and balancing exploration and exploitation. Our approach plugs into standard inverse problem solvers and supports black-box, non-differentiable reward functions. We demonstrate that inference-time search with side information yields substantial gains even with moderate compute ($N=4$) (Fig. 1, left), whereas without side information, scaling provides negligible improvement, as seen in Best-of-N without side information (Fig. 1, right).

- **Experiments:** We evaluate across linear and nonlinear inverse problems (e.g., box inpainting, super-resolution, and motion/Gaussian/nonlinear deblurring) and multiple side information types (reference images, textual descriptions, and MRI). Applying our method to several diffusion-based inverse problem solvers (DPS [Chung et al., 2023b], Blind DPS [Chung et al., 2023a], DAPS [Zhang et al., 2025], and MPGD [He et al., 2024]) we show consistent improvements in perceptual reconstruction quality over all baselines.
- **Ablation:** We provide extensive ablation studies demonstrating robustness to the choice of reward function (Appendix C.10), side information quality (Appendix C.6.2), and the resampling hyperparameter B across a range of values (Appendix C.11). Our experiments further confirm that the reward-tilted posterior approximation produces samples consistent with the ground-truth posterior, and that scaling inference-time compute *without* side information fails to improve, or can even degrade, reconstruction quality (Table 8), justifying the additional compute cost.

2 Related work

Inverse problems with diffusion priors: Diffusion models [Dhariwal and Nichol, 2021, Ho et al., 2020, Song and Ermon, 2019, Sohl-Dickstein et al., 2015, Song and Ermon, 2020, Song et al., 2021a] are powerful generative models that sample from data distributions by iteratively denoising random noise. Several works adapt diffusion priors to inverse problems via likelihood score approximations. Diffusion Posterior Sampling (DPS) [Chung et al., 2023b] is a foundational method for solving inverse problems in a principled way. Its key idea is to approximate the expected conditional likelihood by evaluating the likelihood at the conditional mean. Recent work has focused on improving performance by leveraging the manifold constraints [He et al., 2024] and by decoupling diffusion steps [Zhang et al., 2025]. Latent diffusion priors are also used: PSLD [Rout et al., 2023] adds consistency terms, ReSample [Song et al., 2024] solves per-step optimization problems, and Chung et al. [2024] tunes prompts for efficiency. *None of these methods, however, leverage side information.*

Inverse problems with side information: Many works in signal processing [Mota et al., 2017, Oymak et al., 2013, Jones, 2009, Chun et al., 2012, Ehrhardt et al., 2014, Hyder et al., 2019] integrate structural correlations from auxiliary signals, often via designing appropriate optimization algorithms. Diffusion-based approaches include training with joint priors across modalities [Levac et al., 2023, Efimov et al., 2025], metadata conditioning [Chung et al., 2025], and text-guided regularization [Kim et al., 2025a]. In MRI, LeSITA [Tsiligianni and Deligiannis, 2019] learns coupled sparse representations, and TGVN [Atalik et al., 2025] constrains ambiguous subspaces with additional contrasts using learned unrolled networks. Most approaches, however, are training-based or bound to one modality of side information associated with the trained conditional diffusion model.

Inference-time search: Reward-guided inference-time search has advanced LLM reasoning using Process Advantage Verifiers (PAVs) [Setlur et al., 2025], compute-optimal scheduling [Snell et al., 2025], and reward-guided small models [Liu et al., 2025]. Some recent works [Singhal et al., 2025, Li et al., 2025] apply reward-based search in diffusion for text-to-image/protein generation, but do not consider side information or inverse problems.

Other related work: A detailed additional related work is provided in Appendix Section A.

3 Preliminaries and Problem Formulation

3.1 Preliminaries

Diffusion models: Diffusion models [Ho et al., 2020, Song et al., 2021b] are powerful generative models in which a neural network learns to reverse a forward process that progressively corrupts samples from p_{data} with Gaussian noise, enabling generation by iterative denoising. The forward process is represented by the stochastic differential equation (SDE), $d\mathbf{x}_t = f(\mathbf{x}_t, t)dt + g(t)d\mathbf{w}_t$, $\forall t \in [0, T]$, where \mathbf{w}_t is a Wiener process. Common choices for f, g are $f(\mathbf{x}_t, t) = -(\beta(t)/2)\mathbf{x}_t$ and $g(t) = \sqrt{\beta(t)}$ for non-negative monotonically increasing $\beta(\cdot)$. The corresponding reverse process of this SDE is described by [Anderson, 1982, Song et al., 2021b] $d\mathbf{x}_t = (f(\mathbf{x}_t, t) - g^2(t)\nabla_{\mathbf{x}_t} \log p_t(\mathbf{x}_t)) dt + d\mathbf{w}_t$, $\forall t \in [T, 0]$,

where p_t is the marginal of \mathbf{x}_t , $\mathbf{x}_T \sim \mathcal{N}(0, I)$, and $\nabla_{\mathbf{x}_t} \log p_t(\mathbf{x}_t)$ represents the *score function*. Since p_t is unknown, the score function is approximated by a neural network $\mathcal{D}_\theta(\mathbf{x}_t, t)$ via score-matching. In practice, the SDE is discretized into T steps with $\alpha_t \triangleq \prod_{s=1}^t (1 - \beta_s)$.

Solving inverse problems using diffusion models: An inverse problem consists of recovering an unknown signal \mathbf{x}_0 from noisy, partial observations $\mathbf{y} = \mathbf{A}(\mathbf{x}_0) + \sigma_y \mathbf{z}$, where \mathbf{A} is the measurement model, σ_y is the observation noise level, and \mathbf{z} is typically a Gaussian noise. Often, \mathbf{A} is non-injective, making the problem ill-posed. A standard approach is Bayesian: assume a prior p_0 over the signal \mathbf{x}_0 and sample from the posterior $\mathbf{x}_0 \sim p_{0|Y}(\cdot | \mathbf{y})$. Though $p_{0|Y}$ is unknown, sampling can be achieved by replacing the score function in the backward SDE with the conditional score function $\nabla_{\mathbf{x}_t} \log p_{t|Y}(\mathbf{x}_t | \mathbf{y})$. Using Bayes’ theorem, $\nabla_{\mathbf{x}_t} \log p_{t|Y}(\mathbf{x}_t | \mathbf{y}) = \nabla_{\mathbf{x}_t} \log p_t(\mathbf{x}_t) + \nabla_{\mathbf{x}_t} \log p_{Y|t}(\mathbf{y} | \mathbf{x}_t)$.

While the score function network \mathcal{D}_θ of the pre-trained diffusion model can be used to approximate the first term, approximating the second term is significantly more challenging, and numerous approaches [Daras et al., 2024] have addressed this challenge. In particular, Diffusion Posterior Sampling (DPS) [Chung et al., 2023b] proposes a simple approach to approximate $p_{Y|t}$ as $p_{Y|t}(\mathbf{y} | \mathbf{x}_t) = \mathbb{E}_{\mathbf{x}_0 \sim p_{0|t}(\cdot | \mathbf{x}_t)}[p_{Y|0}(\mathbf{y} | \mathbf{x}_0)] \approx p_{Y|0}(\mathbf{y} | \mathbb{E}_{\mathbf{x}_0 \sim p_{0|t}(\cdot | \mathbf{x}_t)}[\mathbf{x}_0])$, by pushing the expectation inside the nonlinear $p_{Y|0}(\mathbf{y} | \cdot)$. The remaining challenge is to compute the conditional mean $\mathbb{E}_{\mathbf{x}_0 \sim p_{0|t}(\cdot | \mathbf{x}_t)}[\mathbf{x}_0] \triangleq \hat{\mathbf{x}}_{0|t}(\mathbf{x}_t)$, which is typically tackled by using Tweedie’s formula [Efron, 2011], leveraging the fact that \mathbf{x}_t given \mathbf{x}_0 is Gaussian. This results in the estimate $\hat{\mathbf{x}}_{0|t}(\mathbf{x}_t) = (1/\sqrt{\alpha_t})(\mathbf{x}_t + (1 - \alpha_t)\nabla_{\mathbf{x}_t} \log p_t(\mathbf{x}_t)) \approx (1/\sqrt{\alpha_t})(\mathbf{x}_t + (1 - \alpha_t)\mathcal{D}_\theta(\mathbf{x}_t, t))$.

3.2 Problem formulation: solving inverse problems with side information

In many applications, the observation \mathbf{y} alone is insufficient to identify the latent signal \mathbf{x}_0 ; auxiliary side information \mathbf{s} (e.g., a reference image, identity/text embedding, or physics-derived features) can dramatically reduce ambiguity. Formally, when side information \mathbf{s} is available, *the goal is to sample from the target conditional distribution* $p_{0|Y,S}(\cdot | \mathbf{y}, \mathbf{s})$. A seemingly direct route is to *train a conditional diffusion model* that accepts \mathbf{s} as input, learn the conditional score function $\nabla_{\mathbf{x}_t} \log p_{t|S}(\mathbf{x}_t | \mathbf{s})$, and then approximate the full conditional score $\nabla_{\mathbf{x}_t} \log p_{t|Y,S}(\mathbf{x}_t | \mathbf{y}, \mathbf{s}) = \nabla_{\mathbf{x}_t} \log p_{t|S}(\mathbf{x}_t | \mathbf{s}) + \nabla_{\mathbf{x}_t} \log p_{Y|t,S}(\mathbf{y} | \mathbf{x}_t, \mathbf{s})$ through a DPS-style method for the second term, to run the backward SDE. However, this training-based approach is impractical: it demands large paired datasets $(\mathbf{x}_0, \mathbf{s})$, which are expensive or impossible to curate; it locks the solver to the training modality of \mathbf{s} ; and general multi-modal conditioning requires prohibitive data and compute. These constraints motivate a training-free alternative that reuses strong unconditional diffusion priors and uses \mathbf{s} only at inference, preserving modality-agnosticism and avoiding costly data collection.

Designing such a training-free method is technically challenging. First, DPS-style derivations rely on tractable likelihoods (e.g., Gaussian $p_{Y|0}$), whereas realistic $p_{S|0}$ are often non-Gaussian, complicating conditional-score construction. Second, even for measurement-only guidance, DPS-style algorithms require back-propagating through the denoiser at every step. Naively extending to side information forces second-order/Hessian terms through the diffusion network. Third, purely gradient-guided diffusion is brittle: it struggles with non-differentiable or black-box rewards, amplifies early-step errors, and can drift off the data manifold. Inference-time search, which has shown remarkable gains in LLMs [Setlur et al., 2025, Liu et al., 2025, Snell et al., 2025] and text-conditioned diffusion [Singhal et al., 2025, Kim et al., 2025b], but not yet in inverse problems, offer a promising path to overcome these challenges. In this context, we address the following questions:

- (i) *Modeling:* How can we realize $p_{0|Y,S}$ at inference time, without any retraining, by constructing a surrogate objective that is valid across diverse side-information modalities?
- (ii) *Algorithm:* How can we design a plug-and-play inference-time search module that is modality-agnostic, compute-aware, and capable of making global corrections (beyond local gradient steps)?

4 Modeling and Algorithm

4.1 Modeling side information using reward function

Given a side-information signal \mathbf{s} corresponding to an unknown \mathbf{x}_0 , and two candidate reconstructions, \mathbf{x}_0^1 and \mathbf{x}_0^2 , a principled way to decide which reconstruction is more truthful is to compare the (unknown) conditional probabilities $p_{0|S}(\mathbf{x}_0^1 | \mathbf{s})$ and $p_{0|S}(\mathbf{x}_0^2 | \mathbf{s})$. Directly estimating $p_{0|S}$ is intractable: it is typically non-Gaussian, multi-modal, and modality dependent. We therefore introduce a reward function $r : \mathbb{R}^d \times \mathcal{S} \rightarrow \mathbb{R}$ that orders reconstructions given \mathbf{s} : if $r(\mathbf{x}_0^1, \mathbf{s}) > r(\mathbf{x}_0^2, \mathbf{s})$, then \mathbf{x}_0^1 is deemed more compatible with \mathbf{x}_0 than \mathbf{x}_0^2 . This abstraction aligns with many real-world applications (as shown in our experiments): when \mathbf{s} is a text description of the target

image \mathbf{x}_0 , we can use a pre-trained text-image model to score text-image alignment. When \mathbf{s} is a reference image of the same entity (e.g., the same person under different poses/lighting), we can use a pre-trained network to score identity similarity. Such rewards are typically available and serve as practical surrogates for $p_{0|S}$ without requiring an explicit conditional density model.

Our key modeling choice is to use $r(\cdot, \mathbf{s})$ to implicitly characterize $p_{0|S}(\cdot | \mathbf{s})$ by tilting the unconditional prior p_0 toward higher-reward regions. Our approach is inspired by LLM alignment [Ouyang et al., 2022, Rafailov et al., 2023], where generation is steered toward high-reward samples without deviating too much from the pre-trained prior p_0 . This is typically formalized as a KL-regularized reward maximization problem, $\max_{p \in \mathcal{P}} (\mathbb{E}_{\mathbf{x} \sim p} [r(\mathbf{x})] - \tau D_{\text{KL}}(p \| p_0))$, where $\tau > 0$ offers the trade-off between the deviation from the prior and reward maximization. This optimization problem admits a closed-form solution, $p^*(\mathbf{x}) \propto p_0(\mathbf{x}) \exp(r(\mathbf{x})/\tau)$ [Rafailov et al., 2023]. Based on this, we *define* our tractable surrogate for $p_{0|S}$ as

$$p_{0|S}(\mathbf{x}_0 | \mathbf{s}) \propto p_0(\mathbf{x}_0) \exp\left(\frac{r(\mathbf{x}_0; \mathbf{s})}{\tau}\right), \quad (1)$$

This assumption: (i) preserves the powerful unconditional diffusion prior p_0 , (ii) injects modality-agnostic side information via a reward, and (iii) produces a tractable objective that we can combine with the measurement model to target $p_{0|Y,S}$ at inference time using a pre-trained diffusion model. We do not claim optimality of Eq. (1); rather, we show it leads to a practical, training-free algorithm that consistently improves reconstructions over strong baselines while keeping compute comparable. We now leverage Eq. (1) to compute the conditional posteriors for the reverse diffusion.

Proposition 1. *Let $p_{t|t+1,Y,S}$ denote the conditional posterior distribution for the reverse diffusion process. Then using Eq. (1) we have*

$$p_{t|t+1,Y,S}(\mathbf{x}_t | \mathbf{x}_{t+1}, \mathbf{y}, \mathbf{s}) \propto p_{t|t+1,Y}(\mathbf{x}_t | \mathbf{x}_{t+1}, \mathbf{y}) \exp(V_t^\tau(\mathbf{x}_t; \mathbf{s}, \mathbf{y})), \quad (2)$$

$$p_{t|Y,S}(\mathbf{x}_t | \mathbf{y}, \mathbf{s}) \propto p_{t|Y}(\mathbf{x}_t | \mathbf{y}) \exp(V_t^\tau(\mathbf{x}_t; \mathbf{s}, \mathbf{y})), \quad (3)$$

where the value function is given by $V_t^\tau(\mathbf{x}_t; \mathbf{s}, \mathbf{y}) \triangleq \log \mathbb{E}_{\mathbf{x}_0 \sim p_{0|t,Y}(\cdot | \mathbf{x}_t, \mathbf{y})} [\exp(r(\mathbf{x}_0; \mathbf{s})/\tau)]$.

The proof is provided in Appendix B.1. Using Eq. (3), we can get the conditional score function as,

$$\nabla_{\mathbf{x}_t} \log p_{t|Y,S}(\mathbf{x}_t | \mathbf{y}, \mathbf{s}) = \nabla_{\mathbf{x}_t} \log p_t(\mathbf{x}_t) + \nabla_{\mathbf{x}_t} \log p_{Y|t}(\mathbf{y} | \mathbf{x}_t) + \nabla_{\mathbf{x}_t} V_t^\tau(\mathbf{x}_t; \mathbf{s}, \mathbf{y}). \quad (4)$$

The computation of V_t^τ is not straightforward. So, we use a DPS-style approximation as $V_t^\tau(\mathbf{x}_t; \mathbf{s}, \mathbf{y}) = \log \mathbb{E}_{\mathbf{x}_0 \sim p_{0|t,Y}(\cdot | \mathbf{x}_t, \mathbf{y})} [\exp(r(\mathbf{x}_0; \mathbf{s})/\tau)] \approx r(\mathbb{E}_{\mathbf{x}_0 \sim p_{0|t,Y}(\cdot | \mathbf{x}_t, \mathbf{y})} [\mathbf{x}_0]; \mathbf{s})/\tau = r(\hat{\mathbf{x}}_{0|t,Y}(\mathbf{x}_t, \mathbf{y}); \mathbf{s})/\tau$. Using some approximation and the fact that $p_{Y|0}$ is Gaussian, we can get

$$\hat{\mathbf{x}}_{0|t,Y}(\mathbf{x}_t, \mathbf{y}) \approx \hat{\mathbf{x}}_{0|t}(\mathbf{x}_t) - (1 - \alpha_t)(\sqrt{\alpha_t})\eta \nabla_{\mathbf{x}_t} \|\mathbf{y} - \mathbf{A}\hat{\mathbf{x}}_{0|t}(\mathbf{x}_t)\|_2^2, \quad (5)$$

$$V_t^\tau(\mathbf{x}_t; \mathbf{s}, \mathbf{y}) \approx \hat{V}_t^\tau(\mathbf{x}_t; \mathbf{s}, \mathbf{y}) \triangleq r(\hat{\mathbf{x}}_{0|t,Y}(\mathbf{x}_t, \mathbf{y}); \mathbf{s})/\tau. \quad (6)$$

Appendix B.2 details the steps leading to Eq. (5)–Eq. (6), and provides a bound on the approximation error $|V_t^\tau(\mathbf{x}_t; \mathbf{s}, \mathbf{y}) - \hat{V}_t^\tau(\mathbf{x}_t; \mathbf{s}, \mathbf{y})|$ in Theorem 3.

We can now get $\nabla_{\mathbf{x}_t} \log p_{t|Y,S}(\mathbf{x}_t | \mathbf{y}, \mathbf{s})$ given in Eq. (4) by replacing $\nabla_{\mathbf{x}_t} V_t^\tau(\mathbf{x}_t; \mathbf{s}, \mathbf{y})$ with $\nabla_{\mathbf{x}_t} \hat{V}_t^\tau(\mathbf{x}_t; \mathbf{s}, \mathbf{y})$. However, running a backward diffusion using $\nabla_{\mathbf{x}_t} \hat{V}_t^\tau(\mathbf{x}_t; \mathbf{s}, \mathbf{y})$ is computationally infeasible because it involves computing second-order derivatives through the denoiser network (Eqs. (5)–(6)). This issue, however, can be circumvented by making a further approximation, by setting $\eta = 0$ in Eq. (5) to get $\hat{\mathbf{x}}_{0|t,Y}(\mathbf{x}_t, \mathbf{y}) \approx \hat{\mathbf{x}}_{0|t}(\mathbf{x}_t)$, which leads to the approximation $\nabla_{\mathbf{x}_t} V_t^\tau(\mathbf{x}_t; \mathbf{s}, \mathbf{y}) \approx \nabla_{\mathbf{x}_t} r(\hat{\mathbf{x}}_{0|t}(\mathbf{x}_t); \mathbf{s})$. We show that the approximation error remains small when t is small even when $\eta = 0$, see Appendix B.2 and Section B.2.1. This approach then reduces to the **reward gradient guidance (RGG)** approach used for the inference-time alignment of diffusion models [Bansal et al., 2024, Kim et al., 2025b, Yu et al., 2023, He et al., 2024], with the critical difference being that the guidance is from both \mathbf{s} and \mathbf{y} .

The RGG approach, however, is limited only to differentiable rewards, and calculating a gradient through the denoiser network at each step of the backward diffusion is computationally intensive. Moreover, RGG is highly sensitive to the hyperparameter, leading to limited performance improvements and undesirable artifacts in the reconstructed images, as illustrated in Section C.7. This motivates a gradient-free approach for leveraging the side information in inverse problems.

4.2 Inference-Time Search Algorithms for Inverse Problems

Inference-time search have recently gained popularity in LLMs [Snell et al., 2025, Setlur et al., 2025, Liu et al., 2025]. Search algorithms solve a multi-step decision-making problem, balancing exploration and exploitation. While Monte Carlo Tree Search (MCTS) [Kocsis and Szepesvári, 2006] was successful in large-scale reinforcement learning systems like AlphaGo [Silver et al., 2016], they are infeasible for diffusion models: estimating the expected reward of a noisy state \mathbf{x}_t requires repeated rollouts. Using a value function to guide the search is an alternative, but this requires significant additional training for each modality of side information. These limitations motivate training-free, computationally tractable inference-time methods.

Particle-based procedures offer one such approach, using the distribution given by Eq. (2), where the value function is replaced by the approximation in Eq. (6). At a given step, suppose we have N samples $\mathbf{x}_{t+1}[1], \dots, \mathbf{x}_{t+1}[N] \sim p_{t+1|Y,S}$. One way to generate samples from $p_{t+1|Y,S}$ is to (i) propose candidates $\tilde{\mathbf{x}}_t[i] \sim p_{t|t+1,Y}(\cdot | \mathbf{x}_{t+1}[i], \mathbf{y})$, (ii) compute rewards $r[i] = r(\hat{\mathbf{x}}_{0:t,Y}(\tilde{\mathbf{x}}_t[i], \mathbf{y}); \mathbf{s})$ (approximate value) (iii) assign weights $w[i] \propto \exp(r[i]/\tau)$ and resample indices with replacement $I[i] \sim \text{Cat}(w[1 : N])$, and (iv) retain $\mathbf{x}_t[I[i]]$ for the next step. In theory, such particle methods converge to the target distribution as $N \rightarrow \infty$ [Wu et al., 2023, Dou and Song, 2024]. In practice, frequent resampling collapses diversity by repeatedly duplicating high-reward particles, leading to under-exploration of the solution space. This motivates a more balanced resampling strategy.

To address this, we introduce **grouped resampling**: we partition the N particles into groups of size g_t and resample independently within each group, so particles only compete locally. This preserves between-group diversity while still exploiting high-reward particles within each group. Based on how we form these groups, we introduce two search algorithms.

Greedy Search (GS): Here, we use a fixed resampling period B and select $g_t = N$ whenever $t \bmod B = 0$, and $g_t = 1$ otherwise. Greedy Search reduces to the **Best-of-N (BON)** strategy when $B \geq T$, since in that case $g_t = 1$ for all t . Smaller values of B emphasize short-term reward exploitation, while larger values promote exploration. An illustration of Greedy Search, with resampling interval B , is shown in Figure 2, where the particles evolve independently between resampling events and only interact at steps that are multiples of B .

Recursive Fork-Join Search (RFJS):

To balance exploration and exploitation, we propose a hierarchical resampling schedule inspired by how researchers collaborate.

As a PhD student, you meet your immediate collaborators frequently, your research group weekly, and the entire AI community once a year at conferences, and when a larger meeting is scheduled, the smaller one is canceled. We apply the same principle to particles: you have N particles in total. Every B steps, you resample across the entire group. Every $B/2$ steps, you resample within groups of size $N/2$, and so on. Formally, the group size at step t is $g_t = N/2^{j^*}$, where $j^* = \min\{i \geq 0 : t \bmod (B/2^i) = 0\}$.

Smaller groups are resampled more often while larger groups are resampled less frequently, resembling the higher frequency of small group meetings compared to large conferences. Particles within each group search the solution space locally, while keeping distinct groups independent from each other ensures a global search over the space, naturally balancing exploration and exploitation. Figure 2 illustrates this strategy, where resampling frequency decreases as group size increases. We have summarized this inference-time search framework in Algorithm 1 in Appendix B.3.

Our framework is modular: regardless of the choice of search algorithm, it can be used to incorporate side information into the inference process. While any search algorithm can be paired with our framework, we find that RFJS scales better in our setting. Furthermore, RFJS simplifies hyperparameter

Figure 2: Illustration of inference-time search methods. Unlike GS, RFJS preserves diversity via dynamic grouping and within-group resampling, thus balancing exploration and exploitation.

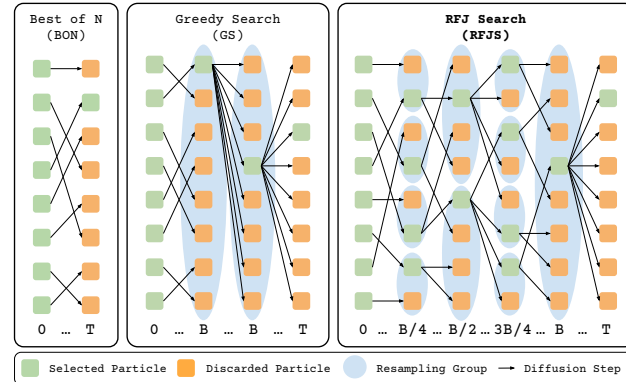
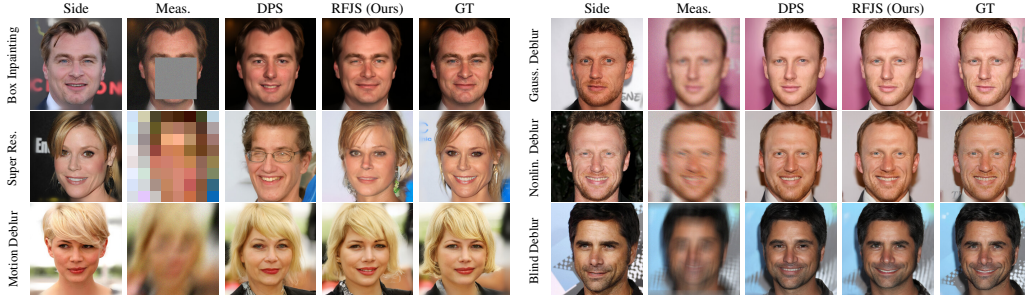


Figure 3: **Image as side information:** Qualitative results using DPS and BlindDPS baseline solvers. In severely ill-posed inverse problems, baseline solvers can fail in identity preservation, while RFJS remains effective; in milder settings, RFJS recovers finer details.



tuning: because it naturally balances exploration and exploitation, τ (used for assigning the weights $w[i]$ for particles) can be set to a sufficiently small value such that selection becomes deterministic, always retaining the particle with the highest reward, without sacrificing performance.

5 Experiments

5.1 Experimental Setup

We evaluate our inference-time search framework for solving inverse problems with side information by instantiating two search algorithms we proposed: **Greedy Search (GS)** and **Recursive Fork Join Search (RFJS)**. We consider two types of side information: (i) **image side information**, a reference image of the same entity (e.g., the same person under different poses or lighting), and (ii) **text side information**, a textual description of the target image.

We demonstrate the plug-and-play nature of our algorithms by considering four different baseline inverse problem solvers: (i) **DPS** [Chung et al., 2023b], (ii) **BlindDPS** [Chung et al., 2023a], (iii) **DAPS** [Zhang et al., 2025], and (iv) **MPGD** [He et al., 2024] (**deferred to Appendix C, due to space constraints**).

Tasks: We consider six inverse problems, covering both linear: (i) box inpainting, (ii) super resolution, (iii) motion deblur, (iv) Gaussian deblur, and nonlinear: (v) nonlinear deblur, (vi) blind deblur. See Appendix D for details.

Baselines: We compare the performance of GS and RFJS against the following baselines: (i) *Baseline solvers (DPS, BlindDPS, MPGD, DAPS)*, (ii) *Best-of-N (BoN)*, which generates N independent samples and selects the one with the best reward at the end, (iii) *Reward Gradient Guidance (RGG)*, which solves the inverse problem by running the backward diffusion according to Eq. (4), but with the approximation $\nabla_{\mathbf{x}_t} V_t^\tau(\mathbf{x}_t; \mathbf{s}, \mathbf{y}) \approx \nabla_{\mathbf{x}_t} r(\hat{\mathbf{x}}_{0|t}(\mathbf{x}_t); \mathbf{s})$. The values of hyperparameters are listed in Appendix D. Experiments are run on NVIDIA A100 GPUs.

5.2 Main Results

Image as side information: The goal is to reconstruct a face image from a noisy observation when another image of the same identity is available (Fig. 3, Fig. 4, Table 1, Table 2). Using CelebA-HQ [Karras et al., 2018] as an out-of-distribution set and a diffusion model pretrained on FFHQ [Chung et al., 2023b], we sample two random images per identity for target and side information. We compute the reward as follows: first, detect the face using MTCNN [Zhang et al., 2016] and then extract identity features with AdaFace [Kim et al., 2022]. Then, we measure the reward as the

Table 1: **Image as side information:** Quantitative results using DPS as the baseline solver. Our algorithms significantly improve perceptual quality as measured by FaceSimilarity (FS), which is more aligned with human perception, while keeping classical metrics (PSNR, SSIM, LPIPS) in a similar range and slightly improving them.

Algorithm	Box Inpainting				Super Resolution ($\times 4$)			
	FS (\downarrow)	PSNR (\uparrow)	LPIPS (\downarrow)	SSIM (\uparrow)	FS (\downarrow)	PSNR (\uparrow)	LPIPS (\downarrow)	SSIM (\uparrow)
RFJS (ours)	0.308	28.29	0.136	0.855	0.380	25.26	0.225	0.695
GS (ours)	0.349	28.22	0.137	0.855	0.460	25.24	0.225	0.696
RGG	0.475	27.96	0.138	0.851	0.573	25.13	0.228	0.690
BoN (w/ side)	0.584	28.20	0.137	0.854	0.915	25.14	0.229	0.694
DPS	0.739	27.93	0.139	0.852	1.042	25.13	0.229	0.693
Algorithm	Non-linear Deblur				Motion Deblur			
	FS (\downarrow)	PSNR (\uparrow)	LPIPS (\downarrow)	SSIM (\uparrow)	FS (\downarrow)	PSNR (\uparrow)	LPIPS (\downarrow)	SSIM (\uparrow)
RFJS (ours)	0.394	23.89	0.229	0.668	0.326	26.64	0.193	0.736
GS (ours)	0.467	23.92	0.232	0.669	0.392	26.58	0.193	0.735
RGG	0.654	23.89	0.231	0.665	0.497	26.55	0.193	0.733
BoN (w/ side)	0.881	23.89	0.233	0.667	0.671	26.57	0.194	0.735
DPS	1.008	23.87	0.232	0.666	0.815	26.54	0.194	0.734
Algorithm	Gaussian Deblur				Blind Deblur			
	FS (\downarrow)	PSNR (\uparrow)	LPIPS (\downarrow)	SSIM (\uparrow)	FS (\downarrow)	PSNR (\uparrow)	LPIPS (\downarrow)	SSIM (\uparrow)
RFJS (ours)	0.330	26.20	0.196	0.712	0.341	25.04	0.209	0.707
GS (ours)	0.385	26.16	0.198	0.711	0.417	25.04	0.211	0.706
RGG	0.495	26.15	0.200	0.709	0.473	24.97	0.211	0.701
BoN (w/ side)	0.667	26.18	0.201	0.711	0.642	25.15	0.210	0.708
DPS	0.807	26.15	0.200	0.711	0.779	24.98	0.213	0.704

Figure 4: **Image as side information:** Qualitative results with DAPS as baseline solver.

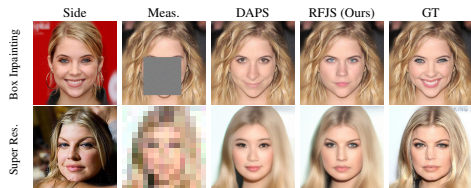


Figure 5: **Text as side information:** Qualitative results using textual side information under severe degradation (e.g., $32\times$ super-resolution with the prompt “golden retriever sitting on a snowy frozen lake, facing forward”). RFJS recovers perceptually meaningful content while DPS fails.



Table 2: **Image as side information:** Quantitative results with DAPS as the baseline solver.

Algorithm	Box Inpainting				Super Resolution ($\times 10$)			
	FS (\downarrow)	PSNR (\uparrow)	LPIPS (\downarrow)	SSIM (\uparrow)	FS (\downarrow)	PSNR (\uparrow)	LPIPS (\downarrow)	SSIM (\uparrow)
RFJS (ours)	0.423	28.720	0.140	0.788	0.654	25.228	0.282	0.661
GS (ours)	0.511	28.640	0.140	0.787	0.760	25.271	0.285	0.662
RGG	0.436	28.410	0.141	0.784	0.579	25.210	0.282	0.659
BON (w/ side)	0.611	28.660	0.141	0.784	0.909	25.220	0.285	0.660
DAPS	0.739	28.290	0.142	0.784	1.020	25.170	0.285	0.659

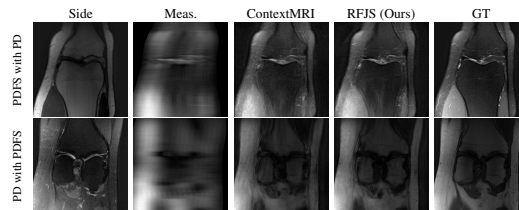
Table 3: **Text as side information:** Quantitative comparison of our algorithms with the baseline. RFJS and GS achieve better performance across all tasks and metrics.

Algorithm	Box Inpainting				Super Resolution ($\times 32$)			
	CS (\uparrow)	PSNR (\uparrow)	SSIM (\uparrow)	LPIPS (\downarrow)	CS (\uparrow)	PSNR (\uparrow)	SSIM (\uparrow)	LPIPS (\downarrow)
RFJS (ours)	0.901	20.75	0.678	0.294	0.801	17.13	0.352	0.493
GS (ours)	0.894	19.76	0.676	0.305	0.791	17.20	0.351	0.509
BON (w/ side)	0.882	19.99	0.672	0.308	0.788	17.21	0.350	0.500
DPS	0.871	19.86	0.672	0.312	0.731	16.90	0.330	0.522

Algorithm	Non-linear Deblur				Motion Deblur			
	CS (\uparrow)	PSNR (\uparrow)	SSIM (\uparrow)	LPIPS (\downarrow)	CS (\uparrow)	PSNR (\uparrow)	SSIM (\uparrow)	LPIPS (\downarrow)
RFJS (ours)	0.863	20.58	0.473	0.405	0.858	18.61	0.402	0.424
GS (ours)	0.865	20.32	0.456	0.405	0.835	17.83	0.369	0.453
BON (w/ side)	0.855	20.52	0.464	0.406	0.848	19.24	0.415	0.427
DPS	0.839	20.55	0.469	0.409	0.794	18.16	0.384	0.458

Algorithm	Gaussian Deblur				Blind Deblur			
	CS (\uparrow)	PSNR (\uparrow)	SSIM (\uparrow)	LPIPS (\downarrow)	CS (\uparrow)	PSNR (\uparrow)	SSIM (\uparrow)	LPIPS (\downarrow)
RFJS (ours)	0.843	18.10	0.358	0.457	0.851	18.84	0.412	0.433
GS (ours)	0.835	17.96	0.356	0.457	0.835	18.93	0.414	0.438
BON (w/ side)	0.831	17.99	0.365	0.452	0.831	18.78	0.410	0.443
DPS	0.778	16.79	0.329	0.487	0.793	18.82	0.409	0.459

Figure 6: **Contrast Image as Side Information:** Qualitative MRI reconstruction with RFJS vs. ContextMRI. The shapes and line edges are well preserved in our reconstruction.



negative of the FaceSimilarity (FS) loss, computed as the distance between the identity embeddings of the reconstructed and side-information faces, extracted by pretrained AdaFace network.

Since standard metrics (PSNR, SSIM, LPIPS) often fail to capture identity similarity, we additionally use FaceSimilarity (FS), which compares the reconstruction to the ground truth for a more reliable measure of identity preservation. Table 1 and Table 2 show that both proposed inference-time search methods, GS and RFJS, outperform baselines (DPS and DAPS respectively), with RFJS achieving the best overall scores. Qualitative results in Fig 3 show sharper facial details and preserve identity. We used $N = 8$ particles and $B = 16$.

Text as side information: The goal is to reconstruct an image from its noisy observation, with a text description of the image available as side information. We use a pre-trained diffusion model trained on the ImageNet data [Dhariwal and Nichol, 2021]. We use 25 images from the ImageNet validation set to evaluate the algorithms and generated a short one-sentence textual description for each image using ChatGPT as the side information. We use ImageReward [Xu et al., 2023], a pre-trained network that measures text-to-image similarity, as the reward function. We consider some inverse problem tasks that are significantly challenging, including $32\times$ super resolution, and strong blur with larger kernels. Experiments use $N=4$ and $B=100$, and we report the standard metrics and CLIPScore [Radford et al., 2021]. CLIPScore measures the cosine similarity between CLIP image embeddings of

the ground truth and reconstruction, providing a semantically informed metric that reflects both visual and textual alignment. The qualitative reconstructions in Fig. 5 closely match the textual descriptions, and the quantitative metrics in Table 3 show that both GS and RFJS outperform competing baselines.

MRI with multi-contrast side information: We use fastMRI knee dataset [Zbontar et al., 2018] with the ContextMRI model [Chung et al., 2025]. We pair PD and PDFS contrasts, reconstructing one from the other under $16\times$ undersampling with 2% ACS. We use normalized mutual information (NMI) as reward, which is robust to contrast changes. Fig. 6 highlights sharper edges and more faithful structure. Table 15 in Appendix D.3 shows our methods consistently improve the baseline.

Role of side information in enabling inference-time scaling: A central contribution of our framework is the principled use of side information through a reward that measures consistency between the reconstruction and the side information at inference time. To see why this is essential, consider the natural alternative: scaling compute via Best-of-N using only the measurement residual $\|y - Ax_0^i\|$ as the selection criterion (BoN w/o SI). When y is

noisy or the inverse problem is ill-posed, this criterion is actively misleading as it favors particles that explain the noise rather than the underlying signal, and as Table 4 shows, performance *can degrade* relative to the baseline. Incorporating side information fundamentally changes this picture: BoN with our reward (BoN w/ SI) draws samples that are more faithful to the conditional posterior $p_{X|Y,S}$, resolving ambiguities that the measurement alone cannot (see Table 8 for more tasks).

Perceptual Quality vs. Classical Metrics: Recent works [Lin et al., 2025, Su et al., 2025] have shown that improvements in perceptual quality for inverse problems do not necessarily translate into better values of classical metrics such as PSNR, SSIM, and LPIPS, and they advocate evaluating with task-specific metrics. In our setting, we use FaceSimilarity for face reconstruction and CLIPScore for ImageNet as task-specific metrics, which are also more aligned with human perceptual judgments for these tasks.

Fig. 7 provides a clear qualitative example of this phenomenon. Although our RFJS reconstruction is more faithful to the ground truth in terms of identity preservation, all three BlindDPS reconstructions achieve better PSNR, SSIM, and LPIPS values. This illustrates that classical metrics can fail to capture meaningful semantic improvements, even when perceptual quality is clearly superior. We provide additional examples and quantitative evidence in Appendix C.1, demonstrating large perceptual gains are not reflected in PSNR, SSIM, or LPIPS.

5.3 Additional Experiments (Appendix)

The results of our framework for other samplers like MPGD, along with additional DPS results, are provided in Appendix C. We further include ablation/sensitivity analyses that address **compute, runtime, robustness, and sensitivity**: (i) **Compute-performance trade-off:** effect of the number of particles (Section C.8). (ii) **Runtime:** wall-clock comparison across methods/settings (Section C.9). (iii) **Robustness:** degradation of **measurement quality** (harder inverse problems) (Section C.6.1) and **side-information quality** (Section C.6.2). (iv) **Sensitivity of Gradient Guidance:** motivating our search-based alternative (Section C.7). (v) **Toy examples:** illustrating the benefits of side information (Section C.12).

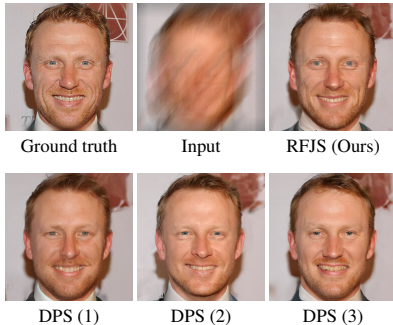
6 Conclusion

We proposed a lightweight, modular inference-time search algorithm that integrates side information into diffusion-based image reconstruction, in a principled way. By adaptively guiding the generative process, our method delivers substantial quality gains, especially in ill-posed settings, while requiring

Table 4: Without side information, Best-of-N selection by $\|y - Ax_0^i\|$ fails to improve over the baseline in noisy settings. With side information, selection by our reward $r(x_0; s)$ consistently improves all metrics.

Algorithm	Box Inpainting				Super Resolution			
	PSNR (\uparrow)	LPIPS (\downarrow)	SSIM (\uparrow)	CS (\uparrow)	PSNR (\uparrow)	LPIPS (\downarrow)	SSIM (\uparrow)	CS (\uparrow)
DAPS	18.21	0.274	0.742	0.855	18.44	0.583	0.391	0.727
BON (w/o SI)	18.02	0.274	0.738	0.846	18.13	0.590	0.368	0.729
BON (w/ SI, ours)	19.51	0.262	0.750	0.893	18.65	0.579	0.398	0.767

Figure 7: Classical metrics fail to capture perceptual fidelity: three BlindDPS reconstructions achieve higher PSNR values (23.5, 23.6, 23.9) than RFJS (23.2), yet RFJS exhibits clearly stronger perceptual similarity to the ground truth. The same pattern holds for LPIPS/SSIM.



only minimal changes to existing pipelines. Extensive experiments across standard reconstruction tasks show consistent improvements in both visual fidelity and quantitative metrics, and our approach surpasses gradient-based alternatives. These results highlight the power of leveraging side information at inference time to make diffusion-based solvers more reliable and accurate.

7 Acknowledgments

We thank the department of Electrical and Computer Engineering (ECEN) at Texas A&M University for providing access to the Olympus computing cluster. Portions of this research were conducted with the advanced computing resources provided by Texas A&M High Performance Research Computing. This work was supported, in part, by the U.S. Army Combat Capabilities Development Command (DEVCOM) under Grant Number W911NF2520046. This work was also supported in part by the National Science Foundation grant NSF-CNS 2148354, federal agencies, and industry partners as specified in the Resilient & Intelligent NextG Systems (RINGS) program. Any opinions, findings, and conclusions or recommendations expressed in this material are those of the authors and do not necessarily reflect the views of the sponsoring agencies.

References

- Brian D.O. Anderson. Reverse-time diffusion equation models. *Stochastic Processes and their Applications*, 12(3):313–326, 1982. ISSN 0304-4149. doi: [https://doi.org/10.1016/0304-4149\(82\)90051-5](https://doi.org/10.1016/0304-4149(82)90051-5). URL <https://www.sciencedirect.com/science/article/pii/0304414982900515>.
- Arda Atalık, Sumit Chopra, and Daniel Sodickson. A Trust-Guided Approach to MR Image Reconstruction with Side Information. *IEEE Transactions on Medical Imaging*, 2025.
- Arpit Bansal, Hong-Min Chu, Avi Schwarzschild, Roni Sengupta, Micah Goldblum, Jonas Geiping, and Tom Goldstein. Universal Guidance for Diffusion Models. In *International Conference on Learning Representations (ICLR)*, 2024.
- Gabriel Cardoso, Yazid Janati el idrissi, Sylvain Le Corff, and Eric Moulines. Monte Carlo guided Denoising Diffusion models for Bayesian linear inverse problems. In *International Conference on Learning Representations (ICLR)*, 2024.
- Se Young Chun, Jeffrey A. Fessler, and Yuni K. Dewaraja. Non-local means methods using ct side information for i-131 spect image reconstruction. In *2012 IEEE Nuclear Science Symposium and Medical Imaging Conference Record (NSS/MIC)*, 2012.
- Hyungjin Chung, Jeongsol Kim, Sehui Kim, and Jong Chul Ye. Parallel Diffusion Models of Operator and Image for Blind Inverse Problems. In *2023 IEEE/CVF Conference on Computer Vision and Pattern Recognition (CVPR)*, 2023a.
- Hyungjin Chung, Jeongsol Kim, Michael Thompson Mccann, Marc Louis Klasky, and Jong Chul Ye. Diffusion posterior sampling for general noisy inverse problems. In *International Conference on Learning Representations (ICLR)*, 2023b.
- Hyungjin Chung, Jong Chul Ye, Peyman Milanfar, and Mauricio Delbracio. Prompt-tuning latent diffusion models for inverse problems. In *Proceedings of the 41st International Conference on Machine Learning*, 2024.
- Hyungjin Chung, Dohun Lee, Zihui Wu, Byung-Hoon Kim, Katherine L Bouman, and Jong Chul Ye. Contextmri: Enhancing compressed sensing mri through metadata conditioning. *arXiv preprint arXiv:2501.04284*, 2025.
- Giannis Daras, Hyungjin Chung, Chieh-Hsin Lai, Yuki Mitsufuji, Jong Chul Ye, Peyman Milanfar, Alexandros G Dimakis, and Mauricio Delbracio. A survey on diffusion models for inverse problems. *arXiv preprint arXiv:2410.00083*, 2024.
- Prafulla Dhariwal and Alexander Nichol. Diffusion models beat gans on image synthesis. In *Advances in Neural Information Processing Systems*, 2021.

- Zehao Dou and Yang Song. Diffusion posterior sampling for linear inverse problem solving: A filtering perspective. In *International Conference on Learning Representations (ICLR)*, 2024.
- Timofey Efimov, Harry Dong, Megna Shah, Jeff Simmons, Sean Donegan, and Yuejie Chi. Leveraging multimodal diffusion models to accelerate imaging with side information. In *IEEE International Conference on Acoustics, Speech and Signal Processing (ICASSP)*, 2025.
- Bradley Efron. Tweedie’s formula and selection bias. *Journal of the American Statistical Association*, 106(496):1602–1614, 2011.
- Matthias J Ehrhardt, Kris Thielemans, Luis Pizarro, David Atkinson, Sébastien Ourselin, Brian F Hutton, and Simon R Arridge. Joint reconstruction of pet-mri by exploiting structural similarity. *Inverse Problems*, 2014.
- Ben Fei, Zhaoyang Lyu, Liang Pan, Junzhe Zhang, Weidong Yang, Tianyue Luo, Bo Zhang, and Bo Dai. Generative diffusion prior for unified image restoration and enhancement. In *Proceedings of the IEEE/CVF conference on computer vision and pattern recognition*, 2023.
- Ian J. Goodfellow, Jonathon Shlens, and Christian Szegedy. Explaining and harnessing adversarial examples. In *International Conference on Learning Representations (ICLR)*, 2015.
- Yutong He, Naoki Murata, Chieh-Hsin Lai, Yuhta Takida, Toshimitsu Uesaka, Dongjun Kim, Wei-Hsiang Liao, Yuki Mitsufuji, J Zico Kolter, Ruslan Salakhutdinov, and Stefano Ermon. Manifold preserving guided diffusion. In *International Conference on Learning Representations (ICLR)*, 2024.
- Jonathan Ho, Ajay Jain, and Pieter Abbeel. Denoising diffusion probabilistic models. In *Advances in Neural Information Processing Systems*, 2020.
- Jonathan Ho, William Chan, Chitwan Saharia, Jay Whang, Ruiqi Gao, Alexey Gritsenko, Diederik P. Kingma, Ben Poole, Mohammad Norouzi, David J. Fleet, and Tim Salimans. Imagen video: High definition video generation with diffusion models. *arXiv preprint arXiv:2210.02303*, 2022.
- Rakib Hyder, Chinmay Hegde, and M. Salman Asif. Fourier phase retrieval with side information using generative prior. In *2019 53rd Asilomar Conference on Signals, Systems, and Computers*, 2019.
- Yazid Janati, Badr MOUFAD, Alain Oliviero Durmus, Eric Moulines, and Jimmy Olsson. Divide-and-conquer posterior sampling for denoising diffusion priors. In *Advances in Neural Information Processing Systems (NeurIPS)*, 2024.
- Lee K. Jones. Local minimax learning of functions with best finite sample estimation error bounds: Applications to ridge and lasso regression, boosting, tree learning, kernel machines, and inverse problems. *IEEE Transactions on Information Theory*, 2009.
- Tero Karras, Timo Aila, Samuli Laine, and Jaakko Lehtinen. Progressive growing of GANs for improved quality, stability, and variation. In *International Conference on Learning Representations (ICLR)*, 2018.
- Jeongsol Kim, Geon Yeong Park, Hyungjin Chung, and Jong Chul Ye. Regularization by texts for latent diffusion inverse solvers. In *International Conference on Learning Representations (ICLR)*, 2025a.
- Minchul Kim, Anil K Jain, and Xiaoming Liu. Adaface: Quality adaptive margin for face recognition. In *Proceedings of the IEEE/CVF Conference on Computer Vision and Pattern Recognition*, 2022.
- Sunwoo Kim, Minkyu Kim, and Dongmin Park. Test-time Alignment of Diffusion Models without Reward Over-optimization. In *International Conference on Learning Representations (ICLR)*, 2025b.
- Levente Kocsis and Csaba Szepesvári. Bandit based monte-carlo planning. In *Proceedings of the 17th European Conference on Machine Learning*, 2006.

- Zhifeng Kong, Wei Ping, Jiaji Huang, Kexin Zhao, and Bryan Catanzaro. Diffwave: A versatile diffusion model for audio synthesis. In *International Conference on Learning Representations (ICLR)*, 2021.
- Brett Levac, Ajil Jalal, Kannan Ramchandran, and Jonathan I. Tamir. MRI Reconstruction with Side Information using Diffusion Models. *2023 57th Asilomar Conference on Signals, Systems, and Computers*, 2023.
- Xiner Li, Masatoshi Uehara, Xingyu Su, Gabriele Scalia, Tommaso Biancalani, Aviv Regev, Sergey Levine, and Shuiwang Ji. Dynamic search for inference-time alignment in diffusion models. *arXiv preprint arXiv:2503.02039*, 2025.
- Tianyu Lin, Xinran Li, Chuntung Zhuang, Qi Chen, Yuanhao Cai, Kai Ding, Alan L. Yuille, and Zongwei Zhou. Are pixel-wise metrics reliable for sparse-view computed tomography reconstruction?, 2025. URL <https://arxiv.org/abs/2506.02093>.
- Runze Liu, Junqi Gao, Jian Zhao, Kaiyan Zhang, Xiu Li, Biqing Qi, Wanli Ouyang, and Bowen Zhou. Can 1b llm surpass 405b llm? rethinking compute-optimal test-time scaling. *arXiv preprint arXiv:2502.06703*, 2025.
- João F. C. Mota, Nikos Deligiannis, and Miguel R. D. Rodrigues. Compressed sensing with prior information: Strategies, geometry, and bounds. *IEEE Transactions on Information Theory*, 2017.
- Long Ouyang, Jeffrey Wu, Xu Jiang, Diogo Almeida, Carroll Wainwright, Pamela Mishkin, Chong Zhang, Sandhini Agarwal, Katarina Slama, Alex Ray, John Schulman, Jacob Hilton, Fraser Kelton, Luke Miller, Maddie Simens, Amanda Askell, Peter Welinder, Paul F Christiano, Jan Leike, and Ryan Lowe. Training language models to follow instructions with human feedback. In *Advances in Neural Information Processing Systems*, 2022.
- Samet Oymak, Christos Thrampoulidis, and Babak Hassibi. Simple bounds for noisy linear inverse problems with exact side information. *arXiv preprint arXiv:1312.0641*, 2013.
- Kushagra Pandey, Farrin Marouf Sofian, Felix Draxler, Theofanis Karaletsos, and Stephan Mandt. Variational control for guidance in diffusion models. In *International Conference on Machine Learning (ICML)*, 2025.
- Alec Radford, Jong Wook Kim, Chris Hallacy, Aditya Ramesh, Gabriel Goh, Sandhini Agarwal, Girish Sastry, Amanda Askell, Pamela Mishkin, Jack Clark, et al. Learning transferable visual models from natural language supervision. In *International conference on machine learning*, 2021.
- Rafael Rafailov, Archit Sharma, Eric Mitchell, Christopher D Manning, Stefano Ermon, and Chelsea Finn. Direct Preference Optimization: Your Language Model is Secretly a Reward Model. In *Advances in Neural Information Processing Systems*, 2023.
- Robin Rombach, Andreas Blattmann, Dominik Lorenz, Patrick Esser, and Bjorn Ommer. High-Resolution Image Synthesis with Latent Diffusion Models . In *2022 IEEE/CVF Conference on Computer Vision and Pattern Recognition (CVPR)*, 2022.
- Litu Rout, Negin Raoof, Giannis Daras, Constantine Caramanis, Alex Dimakis, and Sanjay Shakkottai. Solving linear inverse problems provably via posterior sampling with latent diffusion models. In *Advances in Neural Information Processing Systems*, 2023.
- Litu Rout, Yujia Chen, Nataniel Ruiz, Abhishek Kumar, Constantine Caramanis, Sanjay Shakkottai, and Wen-Sheng Chu. RB-modulation: Training-free stylization using reference-based modulation. In *International Conference on Learning Representations (ICLR)*, 2025.
- Subham Sekhar Sahoo, Marianne Arriola, Yair Schiff, Aaron Gokaslan, Edgar Marroquin, Justin T Chiu, Alexander Rush, and Volodymyr Kuleshov. Simple and effective masked diffusion language models. In *Advances in Neural Information Processing Systems*, 2024.
- Amrith Setlur, Chirag Nagpal, Adam Fisch, Xinyang Geng, Jacob Eisenstein, Rishabh Agarwal, Alekh Agarwal, Jonathan Berant, and Aviral Kumar. Rewarding progress: Scaling automated process verifiers for LLM reasoning. In *International Conference on Learning Representations (ICLR)*, 2025.

- David Silver, Aja Huang, Chris J Maddison, Arthur Guez, Laurent Sifre, George Van Den Driessche, Julian Schrittwieser, Sergey Ioffe, Alan Green, Xi Chen, and et al. Mastering the game of go with deep neural networks and tree search. *Nature*, 2016.
- Raghav Singhal, Zachary Horvitz, Ryan Teehan, Mengye Ren, Zhou Yu, Kathleen Mckeown, and Rajesh Ranganath. A general framework for inference-time scaling and steering of diffusion models. In *International Conference on Machine Learning*, 2025.
- Charlie Victor Snell, Jaehoon Lee, Kelvin Xu, and Aviral Kumar. Scaling LLM test-time compute optimally can be more effective than scaling parameters for reasoning. In *International Conference on Learning Representations (ICLR)*, 2025.
- Jascha Sohl-Dickstein, Eric Weiss, Niru Maheswaranathan, and Surya Ganguli. Deep unsupervised learning using nonequilibrium thermodynamics. In *Proceedings of the 32nd International Conference on Machine Learning*, 2015.
- Bowen Song, Soo Min Kwon, Zecheng Zhang, Xinyu Hu, Qing Qu, and Liyue Shen. Solving inverse problems with latent diffusion models via hard data consistency. In *International Conference on Learning Representations (ICLR)*, 2024.
- Jiaming Song, Chenlin Meng, and Stefano Ermon. Denoising Diffusion Implicit Models. In *International Conference on Learning Representations (ICLR)*, 2021a.
- Jiaming Song, Qinsheng Zhang, Hongxu Yin, Morteza Mardani, Ming-Yu Liu, Jan Kautz, Yongxin Chen, and Arash Vahdat. Loss-Guided Diffusion Models for Plug-and-Play Controllable Generation. In *Proceedings of the 40th International Conference on Machine Learning*, 2023.
- Yang Song and Stefano Ermon. Generative modeling by estimating gradients of the data distribution. In *Advances in Neural Information Processing Systems*, 2019.
- Yang Song and Stefano Ermon. Improved techniques for training score-based generative models. In *Advances in Neural Information Processing Systems*, 2020.
- Yang Song, Jascha Sohl-Dickstein, Diederik P Kingma, Abhishek Kumar, Stefano Ermon, and Ben Poole. Score-based generative modeling through stochastic differential equations. In *International Conference on Learning Representations (ICLR)*, 2021b.
- Shaolin Su, Josep M. Rocafort, Danna Xue, David Serrano-Lozano, Lei Sun, and Javier Vazquez-Corral. Rethinking image evaluation in super-resolution, 2025. URL <https://arxiv.org/abs/2503.13074>.
- Evaggelia Tsiligianni and Nikos Deligiannis. Deep Coupled-Representation Learning for Sparse Linear Inverse Problems With Side Information. *IEEE Signal Processing Letters*, 2019.
- Kevin E Wu, Kevin K Yang, Rianne van den Berg, Sarah Alamdari, James Y Zou, Alex X Lu, and Ava P Amini. Protein structure generation via folding diffusion. *Nature communications*, 2024.
- Luhuan Wu, Brian L. Trippe, Christian A Naesseth, John Patrick Cunningham, and David Blei. Practical and asymptotically exact conditional sampling in diffusion models. In *Advances in Neural Information Processing Systems*, 2023.
- Jiazheng Xu, Xiao Liu, Yuchen Wu, Yuxuan Tong, Qinkai Li, Ming Ding, Jie Tang, and Yuxiao Dong. ImageReward: Learning and Evaluating Human Preferences for Text-to-Image Generation. In *Advances in Neural Information Processing Systems*, 2023.
- Jiwen Yu, Yinhuai Wang, Chen Zhao, Bernard Ghanem, and Jian Zhang. FreeDoM: Training-Free Energy-Guided Conditional Diffusion Model. In *2023 IEEE/CVF International Conference on Computer Vision (ICCV)*, 2023.
- Jure Zbontar, Florian Knoll, Anuroop Sriram, Tullie Murrell, Zhengnan Huang, Matthew J Muckley, Aaron Defazio, Ruben Stern, Patricia Johnson, Mary Bruno, et al. fastmri: An open dataset and benchmarks for accelerated mri. *arXiv preprint arXiv:1811.08839*, 2018.

- Bingliang Zhang, Wenda Chu, Julius Berner, Chenlin Meng, Anima Anandkumar, and Yang Song. Improving diffusion inverse problem solving with decoupled noise annealing. In *Proceedings of the IEEE/CVF Conference on Computer Vision and Pattern Recognition (CVPR)*, 2025.
- Kaipeng Zhang, Zhanpeng Zhang, Zhifeng Li, and Yu Qiao. Joint face detection and alignment using multitask cascaded convolutional networks. *IEEE Signal Processing Letters*, 2016.
- Longwen Zhang, Ziyu Wang, Qixuan Zhang, Qiwei Qiu, Anqi Pang, Haoran Jiang, Wei Yang, Lan Xu, and Jingyi Yu. Clay: A controllable large-scale generative model for creating high-quality 3d assets. *ACM Transactions on Graphics (TOG)*, 2024.

Appendices

A Additional Related Work

Reward-gradient guidance: LGD [Song et al., 2023] refines DPS via Monte Carlo estimates, while UGD [Bansal et al., 2024], FreeDoM [Yu et al., 2023], and RB-Modulation [Rout et al., 2025] propose to guide the diffusion with a gradient of the reward function. In addition to being gradient-based approaches, they are typically used for semantic generation tasks rather than inverse problems.

SMC methods: Sequential Monte Carlo approaches [Cardoso et al., 2024, Dou and Song, 2024, Wu et al., 2023] generate and resample particles under tilted distributions, offering gradient-free alternatives. DAS [Kim et al., 2025b] combines resampling with gradients for text-to-image tasks. These methods rely only on the measurement to guide the unconditional sampler and do not exploit side information.

Guidance and side information in diffusion models: Several recent works have explored conditioning, guidance, and optimization strategies for diffusion models, but they differ substantially in whether and how *side information* is incorporated.

CLAY [Zhang et al., 2024] is a conditional generative model for 3D asset synthesis that incorporates text, image views, and simple 3D cues via trained, modality-specific conditioning modules (e.g., cross-attention adapters) within a native 3D diffusion model. While this enables controllable generation, the conditioning signals are integrated through learned modules during training, and the method is not formulated as an inverse problem under a measurement model.

The term side information is also used by Fei et al. [2023], but in a different sense: their setting considers multiple measurements of the same underlying ground truth, where the relationship between measurements and the clean image is either known or can be estimated parametrically. As a result, the additional information can be incorporated through an explicit forward-model-based formulation. In contrast, we consider side information that may come from heterogeneous modalities (e.g., text, reference images, alternative MRI contrasts) with unknown and nonlinear relationships to the target image. Since such relationships are not expressible as forward models, we incorporate side information implicitly via a reward that guides inference-time search, without retraining.

Other inference-time optimization approaches for diffusion models do not incorporate side information. For example, Chung et al. [2024] optimizes latent variables and text-prompt embeddings during inference to better exploit the learned prior, improving alignment with the prompt but relying solely on internal model variables. Similarly, Janati et al. [2024] uses distribution tilting aligned with the measurement via Langevin dynamics, *without incorporating external side information*, and does not perform inference-time search.

Finally, Pandey et al. [2025] proposes a variational framework that optimizes a reward defined with respect to the measurement likelihood and assumes differentiable reward functions. By contrast, we model the relationship between the target image and side information using a reward-tilted posterior and support non-differentiable rewards, enabling flexible integration of arbitrary side information at inference time.

B Proofs

B.1 Proof of Proposition 1

To begin, recall that $p_{0|S}(\mathbf{x}_0|\mathbf{s}) = \frac{1}{Z} p_0(\mathbf{x}_0) e^{\frac{r(\mathbf{x}_0;\mathbf{s})}{\tau}}$. Using Bayes’ rule, we can rewrite this expression as

$$\frac{1}{Z} p_0(\mathbf{x}_0) \exp\left(\frac{r(\mathbf{x}_0;\mathbf{s})}{\tau}\right) = \frac{p_{0,S}(\mathbf{x}_0,\mathbf{s})}{p_S(\mathbf{s})} = \frac{p_{S|0}(\mathbf{s}|\mathbf{x}_0)p_0(\mathbf{x}_0)}{p_S(\mathbf{s})}$$

and we gather that, for \mathbf{s} fixed, $p_{S|0}(\mathbf{s}|\mathbf{x}_0) \propto e^{\frac{r(\mathbf{x}_0;\mathbf{s})}{\tau}}$ where the proportionality is up to constants on independent of \mathbf{x}_0 . Starting from the LHS of (2), we first apply Bayes’ rule, reverse the conditioning,

and introduce a marginalized \mathbf{x}_0 to leverage conditional independence. This sequence leads to

$$\begin{aligned}
p_{t|t+1,Y,S}(\mathbf{x}_t | \mathbf{x}_{t+1}, \mathbf{y}, \mathbf{s}) &= \frac{p_{t,S|t+1,Y}(\mathbf{x}_t, \mathbf{s} | \mathbf{x}_{t+1}, \mathbf{y})}{p_{S|t+1,Y}(\mathbf{s} | \mathbf{x}_{t+1}, \mathbf{y})} \\
&= \frac{p_{t|t+1,Y}(\mathbf{x}_t | \mathbf{x}_{t+1}, \mathbf{y}) p_{S|t,t+1,Y}(\mathbf{s} | \mathbf{x}_t, \mathbf{x}_{t+1}, \mathbf{y})}{p_{S|t+1,Y}(\mathbf{s} | \mathbf{x}_{t+1}, \mathbf{y})} \\
&\propto p_{t|t+1,Y}(\mathbf{x}_t | \mathbf{x}_{t+1}, \mathbf{y}) \int_{\mathbf{x}_0} p_{S|t,t+1,Y}(\mathbf{s} | \mathbf{x}_0, \mathbf{x}_t, \mathbf{x}_{t+1}, \mathbf{y}) p_{0|t,t+1,Y}(\mathbf{x}_0 | \mathbf{x}_t, \mathbf{x}_{t+1}, \mathbf{y}) d\mathbf{x}_0 \\
&= p_{t|t+1,Y}(\mathbf{x}_t | \mathbf{x}_{t+1}, \mathbf{y}) \int_{\mathbf{x}_0} p_{S|0,t,t+1,Y}(\mathbf{s} | \mathbf{x}_0, \mathbf{x}_t, \mathbf{x}_{t+1}, \mathbf{y}) p_{0|t,Y}(\mathbf{x}_0 | \mathbf{x}_t, \mathbf{y}) d\mathbf{x}_0 \\
&\propto p_{t|t+1,Y}(\mathbf{x}_t | \mathbf{x}_{t+1}, \mathbf{y}) \int_{\mathbf{x}_0} p_{S|0}(\mathbf{s} | \mathbf{x}_0) p_{0|t,Y}(\mathbf{x}_0 | \mathbf{x}_t, \mathbf{y}) d\mathbf{x}_0 \\
&= p_{t|t+1,Y}(\mathbf{x}_t | \mathbf{x}_{t+1}, \mathbf{y}) \mathbb{E}_{\mathbf{x}_0 \sim p_{0|t,Y}(\cdot | \mathbf{x}_t, \mathbf{y})} [\exp(r(\mathbf{x}_0; \mathbf{s})/\tau)] \\
&\propto p_{t|t+1,Y}(\mathbf{x}_t | \mathbf{x}_{t+1}, \mathbf{y}) \exp(V_t^\tau(\mathbf{x}_t; \mathbf{s}, \mathbf{y})).
\end{aligned}$$

The penultimate step follows from the discussion at the onset of the proof. The last step captures the definition for $V_t^\tau(\mathbf{x}_t; \mathbf{s}, \mathbf{y})$ found in Proposition 1. The proof of (3) is similar without conditioning on $t + 1$.

Proof of Value-titled KL. Given a distribution p_0 over \mathbb{R}^d , a reward function $r : \mathbb{R}^d \rightarrow \mathbb{R}$, and $\tau > 0$, we are interested in sampling from the distribution p^* given by

$$\begin{aligned}
p^* &= \arg \max_p \mathbb{E}_{\mathbf{x} \sim p} [r(\mathbf{x})] - \tau D_{\text{KL}}(p \| p_0) \\
&= \arg \max_p \mathbb{E}_{\mathbf{x} \sim p} \left[r(\mathbf{x}) - \tau \log \frac{p(\mathbf{x})}{p_0(\mathbf{x})} \right] \\
&= \arg \min_p \mathbb{E}_{\mathbf{x} \sim p} \left[\log \frac{p(\mathbf{x})}{p_0(\mathbf{x})} - \frac{r(\mathbf{x})}{\tau} \right] \\
&= \arg \min_p \mathbb{E}_{\mathbf{x} \sim p} \left[\log \frac{p(\mathbf{x})}{p_0(\mathbf{x}) e^{r(\mathbf{x})/\tau}} \right] \triangleq \arg \min_p \mathcal{L}(p).
\end{aligned}$$

Let $q(\mathbf{x}) \triangleq \frac{1}{Z} p_0(\mathbf{x}) e^{r(\mathbf{x})/\tau}$, where Z is chosen such that $\int q(\mathbf{x}) d\mathbf{x} = 1$. Then

$$\mathcal{L}(p) = \mathbb{E}_{\mathbf{x} \sim p} \left[\log \frac{p(\mathbf{x})}{p_0(\mathbf{x}) e^{r(\mathbf{x})/\tau}} \right] = \mathbb{E}_{\mathbf{x} \sim p} \left[\log \frac{p(\mathbf{x})}{Z q(\mathbf{x})} \right] = D_{\text{KL}}(p \| q) - \log Z.$$

By the non-negativity of KL-divergence, $\mathcal{L}(p) \geq \mathcal{L}(q)$ for any distribution p , and so $p^* = q$, or $p(\mathbf{x}) \propto p_0(\mathbf{x}) e^{r(\mathbf{x})/\tau}$.

B.2 Value Approximation Bound

In the following, we provide the steps that lead to Eq. 6, and subsequently bound the approximation error. We begin with the following lemma.

Lemma 2. *The conditional mean of X_0 given $X_t = \mathbf{x}_t$ and $Y = \mathbf{y}$ is given by*

$$\hat{\mathbf{x}}_{0|t,Y}(\mathbf{x}_t, \mathbf{y}) = \hat{\mathbf{x}}_{0|t}(\mathbf{x}_t) + \left(\frac{1 - \alpha_t}{\sqrt{\alpha_t}} \right) \nabla_{\mathbf{x}_t} \log p_{Y|t}(\mathbf{y} | \mathbf{x}_t). \quad (7)$$

Proof. For any distribution over X_0 since $p_{t|0}(\mathbf{x}_t | \mathbf{x}_0) = \mathcal{N}(\mathbf{x}_t | \sqrt{\alpha_t} \mathbf{x}_0, (1 - \alpha_t) \mathbf{I})$, we can use the Tweedie's formula [Efron, 2011] to $p_{0|Y}(\mathbf{x}_0 | \mathbf{y})$ and $p_0(\mathbf{x}_0)$ to get

$$\begin{aligned}
\sqrt{\alpha_t} \hat{\mathbf{x}}_{0|t,Y}(\mathbf{x}_t, \mathbf{y}) &= \mathbf{x}_t + (1 - \alpha_t) \nabla_{\mathbf{x}_t} \log p_{t|Y}(\mathbf{x}_t | \mathbf{y}) \\
\sqrt{\alpha_t} \hat{\mathbf{x}}_{0|t}(\mathbf{x}_t) &= \mathbf{x}_t + (1 - \alpha_t) \nabla_{\mathbf{x}_t} \log p_t(\mathbf{x}_t).
\end{aligned}$$

Since by Bayes theorem, $\nabla_{\mathbf{x}_t} \log p_{t|Y}(\mathbf{x}_t | \mathbf{y}) = \nabla_{\mathbf{x}_t} \log p_t(\mathbf{x}_t) + \log p_{Y|t}(\mathbf{y} | \mathbf{x}_t)$, the results follows by simple algebra.

Since $p_{Y|0}$ is Gaussian, using the DPS approximation on the second term in Eq. (7), we get

$$\hat{\mathbf{x}}_{0|t,Y}(\mathbf{x}_t, \mathbf{y}) \approx \hat{\mathbf{x}}_{0|t}(\mathbf{x}_t) - \left(\frac{1 - \alpha_t}{\sqrt{\alpha_t}} \right) \frac{1}{2\sigma_y^2} \nabla_{\mathbf{x}_t} \|\mathbf{y} - \mathbf{A}(\hat{\mathbf{x}}_{0|t}(\mathbf{x}_t))\|_2^2.$$

Replacing $1/2\sigma_y^2$ by η to control the approximation error gives Eq. (5). In the following, we denote this approximation as

$$\hat{\mathbf{x}}_{0|t,Y}(\mathbf{x}_t, \mathbf{y}) \approx \hat{\mathbf{x}}_{0|t}(\mathbf{x}_t) - \left(\frac{1 - \alpha_t}{\sqrt{\alpha_t}} \right) \eta \nabla_{\mathbf{x}_t} \|\mathbf{y} - \mathbf{A}(\hat{\mathbf{x}}_{0|t}(\mathbf{x}_t))\|_2^2 \triangleq \tilde{\mathbf{x}}_{0|t}^\eta(\mathbf{x}_t, \mathbf{y}).$$

Proposition 3. Assume that r is a Lipschitz function that takes values in $[0, 1]$. For any $\mathbf{x}_t, \mathbf{y}, \mathbf{s}$, the error in the value approximation $\hat{V}_t^\tau(\mathbf{x}_t; \mathbf{s}, \mathbf{y}) = r(\tilde{\mathbf{x}}_{0|t}^\eta(\mathbf{x}_t, \mathbf{y}); \mathbf{s})/\tau$ with the true value $V_t^\tau(\mathbf{x}_t; \mathbf{s}, \mathbf{y})$ is bounded as

$$|V_t^\tau(\mathbf{x}_t; \mathbf{s}, \mathbf{y}) - \hat{V}_t^\tau(\mathbf{x}_t; \mathbf{s}, \mathbf{y})| \leq c_\tau c_1(t) + \frac{L_r}{\tau} \left(\sqrt{c_2(t)} + \sqrt{c_3(t)c_4^\eta(t)} \right),$$

where $c_1(t) = \text{Var}(r(X_0; \mathbf{s}) \mid \mathbf{x}_t, \mathbf{y})$, $c_2(t) = \text{Var}(X_0 \mid \mathbf{x}_t, \mathbf{y})$, $c_3(t) = \text{Var}(X_0 \mid \mathbf{x}_t)$,

$$c_4^\eta(t) = 1 + \text{CV}^2(t) + \eta^2 \|\mathbf{A}^T(\mathbf{y} - \mathbf{A}\hat{\mathbf{x}}_{0|t}(\mathbf{x}_t))\|_{\Sigma_{0|t}(\mathbf{x}_t)}^2 - 2\eta \langle \mathbf{A}(\hat{\mathbf{x}}_{0|t,Y}(\mathbf{x}_t, \mathbf{y}) - \hat{\mathbf{x}}_{0|t}(\mathbf{x}_t)), \mathbf{y} - \mathbf{A}\hat{\mathbf{x}}_{0|t}(\mathbf{x}_t) \rangle,$$

where $\text{CV}(t) \triangleq \frac{\sqrt{\text{Var}(p_{Y|0}(\mathbf{y}|X_0)|\mathbf{x}_t)}}{\mathbb{E}[p_{Y|0}(\mathbf{y}|X_0)|\mathbf{x}_t]}$ is the coefficient of variation of the likelihood function $p_{Y|0}(\mathbf{y} \mid X_0)$ given \mathbf{x}_t and $c_\tau = e^{1/\tau} - 1 - 1/\tau$ is a positive constant.

Remark 4. In Proposition 3, the term $c_1(t)$ denotes the conditional variance of the reward given \mathbf{x}_t, \mathbf{y} , $c_2(t)$ denotes the conditional variance of X_0 given \mathbf{x}_t, \mathbf{y} , and $c_3(t)$ denotes the conditional variance of X_0 given only \mathbf{x}_t . Since the variance of the reverse distribution $p_{0|t}(\cdot \mid \mathbf{x}_t)$ decreases as t becomes smaller, we have that all the terms $c_1(t), c_2(t), c_3(t)$ are small when t is small. Therefore, the approximation error is small when t is small.

Proof. Since r is a bounded random variable, assuming finite variance, we can use Bennett's inequality for the log moment-generating function

$$V_t^\tau(\mathbf{x}_t; \mathbf{s}, \mathbf{y}) = \log \mathbb{E}[\exp(r(X_0; \mathbf{s})/\tau)] \leq \frac{1}{\tau} \mathbb{E}[r(X_0; \mathbf{s})] + c_\tau c_1(t).$$

Then, we have

$$|\log \mathbb{E}[\exp(r(X_0; \mathbf{s})/\tau)] - \frac{1}{\tau} r(\tilde{\mathbf{x}}_{0|t,Y}^\eta(\mathbf{x}_t, \mathbf{y}))| \leq \frac{1}{\tau} |\mathbb{E}[r(X_0; \mathbf{s})] - r(\tilde{\mathbf{x}}_{0|t,Y}^\eta(\mathbf{x}_t, \mathbf{y}))| + c_\tau c_1(t).$$

Now, let us simplify the first term,

$$\begin{aligned} |\mathbb{E}[r(X_0; \mathbf{s})] - r(\tilde{\mathbf{x}}_{0|t,Y}^\eta(\mathbf{x}_t, \mathbf{y}); \mathbf{s})| &\leq \mathbb{E}[|r(X_0; \mathbf{s}) - r(\tilde{\mathbf{x}}_{0|t,Y}^\eta(\mathbf{x}_t, \mathbf{y}); \mathbf{s})|] \\ &\leq L_r \mathbb{E}[\|X_0 - \tilde{\mathbf{x}}_{0|t,Y}^\eta(\mathbf{x}_t, \mathbf{y})\|_2] \\ &\leq L_r (\mathbb{E}[\|X_0 - \hat{\mathbf{x}}_{0|t,Y}(\mathbf{x}_t, \mathbf{y})\|_2] + \|\hat{\mathbf{x}}_{0|t,Y}(\mathbf{x}_t, \mathbf{y}) - \tilde{\mathbf{x}}_{0|t,Y}^\eta(\mathbf{x}_t, \mathbf{y})\|_2). \end{aligned}$$

The first term can be bounded by $\sqrt{c_2(t)}$ using Cauchy-Schwarz inequality in L^2 -probability space. For the second term, first we simplify

$$\tilde{\mathbf{x}}_{0|t,Y}^\eta(\mathbf{x}_t, \mathbf{y}) = \hat{\mathbf{x}}_{0|t}(\mathbf{x}_t) - \left(\frac{1 - \alpha_t}{\sqrt{\alpha_t}} \right) \eta \nabla_{\mathbf{x}_t} \|\mathbf{y} - \mathbf{A}\hat{\mathbf{x}}_{0|t}(\mathbf{x}_t)\|_2^2,$$

and then $\nabla_{\mathbf{x}_t} \|\mathbf{y} - \mathbf{A}\hat{\mathbf{x}}_{0|t}(\mathbf{x}_t)\|_2^2 = -(\nabla_{\mathbf{x}_t} \hat{\mathbf{x}}_{0|t}(\mathbf{x}_t)) \mathbf{A}^T (\mathbf{y} - \mathbf{A}\hat{\mathbf{x}}_{0|t}(\mathbf{x}_t))$. Now,

$$\begin{aligned} \nabla_{\mathbf{x}_t} \hat{\mathbf{x}}_{0|t}(\mathbf{x}_t) &= \nabla_{\mathbf{x}_t} \int \mathbf{x}_0^T p_{0|t}(\mathbf{x}_0 \mid \mathbf{x}_t) d\mathbf{x}_0 = \int \nabla_{\mathbf{x}_t} p_{0|t}(\mathbf{x}_0 \mid \mathbf{x}_t) \mathbf{x}_0^T d\mathbf{x}_0 \\ &= \int \nabla_{\mathbf{x}_t} \log p_{0|t}(\mathbf{x}_0 \mid \mathbf{x}_t) \mathbf{x}_0^T p_{0|t}(\mathbf{x}_0 \mid \mathbf{x}_t) d\mathbf{x}_0. \end{aligned}$$

Now, we shall compute

$$\nabla_{\mathbf{x}_t} \log p_{0|t}(\mathbf{x}_0 | \mathbf{x}_t) = \nabla_{\mathbf{x}_t} \log p_{t|0}(\mathbf{x}_t | \mathbf{x}_0) - \nabla_{\mathbf{x}_t} \log p_t(\mathbf{x}_t).$$

But since $\sqrt{\alpha_t} \hat{\mathbf{x}}_{0|t}(\mathbf{x}_t) = \mathbf{x}_t + (1 - \alpha_t) \nabla_{\mathbf{x}_t} \log p_t(\mathbf{x}_t)$, and $\nabla_{\mathbf{x}_t} \log p_{t|0}(\mathbf{x}_t | \mathbf{x}_0) = \frac{1}{1 - \alpha_t} (\sqrt{\alpha_t} \mathbf{x}_0 - \mathbf{x}_t)$, which gives

$$\left(\frac{1 - \alpha_t}{\sqrt{\alpha_t}} \right) \nabla_{\mathbf{x}_t} \log p_{0|t}(\mathbf{x}_0 | \mathbf{x}_t) = \mathbf{x}_0 - \hat{\mathbf{x}}_{0|t}(\mathbf{x}_t),$$

which gives

$$\begin{aligned} \left(\frac{1 - \alpha_t}{\sqrt{\alpha_t}} \right) \nabla_{\mathbf{x}_t} \hat{\mathbf{x}}_{0|t}(\mathbf{x}_t) &= \mathbb{E}_{X_0 \sim p_{0|t}(\mathbf{x}_t)} [(X_0 - \hat{\mathbf{x}}_{0|t}(\mathbf{x}_t)) X_0^T] \\ &= \mathbb{E}_{p_{0|t}(\mathbf{x}_t)} [X_0 X_0^T] - \mathbb{E}_{p_{0|t}(\mathbf{x}_t)} [X_0] \mathbb{E}_{p_{0|t}(\mathbf{x}_t)} [X_0^T] \\ &= \mathbb{E}_{p_{0|t}(\mathbf{x}_t)} [(X_0 - \hat{\mathbf{x}}_{0|t}(\mathbf{x}_t))(X_0 - \hat{\mathbf{x}}_{0|t}(\mathbf{x}_t))^T] \triangleq \Sigma_{0|t}(\mathbf{x}_t), \end{aligned}$$

which is precisely the covariance matrix of X_0 given \mathbf{x}_t .

Thus, we finally get,

$$\tilde{\mathbf{x}}_{0|t,Y}^\eta(\mathbf{x}_t, \mathbf{y}) = \hat{\mathbf{x}}_{0|t}(\mathbf{x}_t) + \eta \Sigma_{0|t}(\mathbf{x}_t) \mathbf{A}^T (\mathbf{y} - \mathbf{A} \hat{\mathbf{x}}_{0|t}(\mathbf{x}_t))$$

Next, note that since $\mathbb{E}_{p_{0|t}(\mathbf{x}_t)} [p_{Y|0}(\mathbf{y} | X_0)] = p_{Y|t}(\mathbf{y} | \mathbf{x}_t)$, we can define $f(X_0) = \frac{p_{Y|0}(\mathbf{y} | X_0)}{\mathbb{E}_{p_{0|t}(\mathbf{x}_t)} [p_{Y|0}(\mathbf{y} | X_0)]}$, whose expectation is $\mathbb{E}_{p_{0|t}(\mathbf{x}_t)} [f(X_0)] = 1$. Further, it is easy to see that $\hat{\mathbf{x}}_{0|t,Y}^\eta(\mathbf{x}_t, \mathbf{y}) = \mathbb{E}_{p_{0|t}(\mathbf{x}_t)} [X_0 f(X_0)]$. Now, we are ready to bound the final term as follows

$$\begin{aligned} &\|\hat{\mathbf{x}}_{0|t,Y}^\eta(\mathbf{x}_t, \mathbf{y}) - \tilde{\mathbf{x}}_{0|t,Y}^\eta(\mathbf{x}_t, \mathbf{y})\|_2 \\ &= \|\mathbb{E}_{p_{0|t}(\mathbf{x}_t)} [X_0 f(X_0)] - \hat{\mathbf{x}}_{0|t}(\mathbf{x}_t) - \eta \Sigma_{0|t}(\mathbf{x}_t) \mathbf{A}^T (\mathbf{y} - \mathbf{A} \hat{\mathbf{x}}_{0|t}(\mathbf{x}_t))\|_2 \\ &= \|\mathbb{E}_{p_{0|t}(\mathbf{x}_t)} [X_0 f(X_0) - \hat{\mathbf{x}}_{0|t}(\mathbf{x}_t) f(X_0)] \\ &\quad - \eta \mathbb{E}_{p_{0|t}(\mathbf{x}_t)} [(X_0 - \hat{\mathbf{x}}_{0|t}(\mathbf{x}_t))(X_0 - \hat{\mathbf{x}}_{0|t}(\mathbf{x}_t))^T] \mathbf{A}^T (\mathbf{y} - \mathbf{A} \hat{\mathbf{x}}_{0|t}(\mathbf{x}_t))\|_2 \\ &= \|\mathbb{E}_{p_{0|t}(\mathbf{x}_t)} [(X_0 - \hat{\mathbf{x}}_{0|t}(\mathbf{x}_t))(f(X_0) - \eta(X_0 - \hat{\mathbf{x}}_{0|t}(\mathbf{x}_t))^T \mathbf{A}^T (\mathbf{y} - \mathbf{A} \hat{\mathbf{x}}_{0|t}(\mathbf{x}_t)))]\|_2 \\ &\leq \mathbb{E}_{p_{0|t}(\mathbf{x}_t)} [\|(X_0 - \hat{\mathbf{x}}_{0|t}(\mathbf{x}_t))(f(X_0) - \eta(X_0 - \hat{\mathbf{x}}_{0|t}(\mathbf{x}_t))^T \mathbf{A}^T (\mathbf{y} - \mathbf{A} \hat{\mathbf{x}}_{0|t}(\mathbf{x}_t))\|_2] \\ &= \mathbb{E}_{p_{0|t}(\mathbf{x}_t)} [\|X_0 - \hat{\mathbf{x}}_{0|t}(\mathbf{x}_t)\|_2 |f(X_0) - \eta(X_0 - \hat{\mathbf{x}}_{0|t}(\mathbf{x}_t))^T \mathbf{A}^T (\mathbf{y} - \mathbf{A} \hat{\mathbf{x}}_{0|t}(\mathbf{x}_t))|] \\ &\leq \sqrt{c_3(t)} \sqrt{c_4^\eta(t)}, \end{aligned}$$

where the last step follows by Cauchy-Schwarz inequality in L^2 probability space, where

$$c_3(t) \triangleq \mathbb{E}_{p_{0|t}(\mathbf{x}_t)} [\|X_0 - \mathbb{E}_{p_{0|t}(\mathbf{x}_t)} [X_0]\|_2^2] = \text{Var}(X_0 | \mathbf{x}_t).$$

and at last, we have

$$\begin{aligned} c_4^\eta(t) &\triangleq \mathbb{E}_{p_{0|t}(\mathbf{x}_t)} [(f(X_0) - \eta(X_0 - \hat{\mathbf{x}}_{0|t}(\mathbf{x}_t))^T \mathbf{A}^T (\mathbf{y} - \mathbf{A} \hat{\mathbf{x}}_{0|t}(\mathbf{x}_t)))^2] \\ &= \mathbb{E}_{p_{0|t}(\mathbf{x}_t)} [f(X_0)^2] + \eta^2 \mathbb{E} [((X_0 - \hat{\mathbf{x}}_{0|t}(\mathbf{x}_t))^T \mathbf{A}^T (\mathbf{y} - \mathbf{A} \hat{\mathbf{x}}_{0|t}(\mathbf{x}_t)))^2] \\ &\quad - 2\eta \mathbb{E}_{p_{0|t}(\mathbf{x}_t)} [(X_0 f(X_0) - f(X_0) \hat{\mathbf{x}}_{0|t}(\mathbf{x}_t))^T] \mathbf{A}^T (\mathbf{y} - \mathbf{A} \hat{\mathbf{x}}_{0|t}(\mathbf{x}_t)) \\ &= \mathbb{E}_{p_{0|t}(\mathbf{x}_t)} [f(X_0)^2] + \eta^2 \|\mathbf{A}^T (\mathbf{y} - \mathbf{A} \hat{\mathbf{x}}_{0|t}(\mathbf{x}_t))\|_{\Sigma_{0|t}(\mathbf{x}_t)}^2 \\ &\quad - 2\eta \langle \mathbf{A} (\hat{\mathbf{x}}_{0|t,Y}^\eta(\mathbf{x}_t, \mathbf{y}) - \hat{\mathbf{x}}_{0|t}(\mathbf{x}_t)), \mathbf{y} - \mathbf{A} \hat{\mathbf{x}}_{0|t}(\mathbf{x}_t) \rangle. \end{aligned}$$

Since $\mathbb{E}_{p_{0|t}(\mathbf{x}_t)} [f(X_0)^2] = \frac{\mathbb{E}_{p_{0|t}(\mathbf{x}_t)} [(p_{Y|0}(\mathbf{y} | X_0))^2]}{(\mathbb{E}_{p_{0|t}(\mathbf{x}_t)} [p_{Y|0}(\mathbf{y} | X_0)])^2} = 1 + \text{CV}^2(t)$, where $\text{CV}(t) = \frac{\sqrt{\text{Var}(p_{Y|0}(\mathbf{y} | X_0) | \mathbf{x}_t)}}{\mathbb{E}[p_{Y|0}(\mathbf{y} | X_0) | \mathbf{x}_t]}$ is the coefficient of variation of the likelihood function given \mathbf{x}_t .

B.2.1 Discussion on η

Theorem 3 states that the approximation error is small when t is small. In fact, under the (standard) assumptions, the error goes to 0 irrespective of the value of η . Thus, one can set $\eta = 0$ and still obtain consistent estimate of the conditional mean $\hat{\mathbf{x}}_{0|t,Y}(\mathbf{x}_t, \mathbf{y}) \approx \hat{\mathbf{x}}_{0|t}(\mathbf{x}_t)$ when t is small.

To get an intuitive justification from a simpler theoretical perspective, notice that the measurement $\mathbf{y} = \mathbf{A}\mathbf{x}_0 + \sigma_y \mathbf{z}$ is a noisy observation of \mathbf{x}_0 and \mathbf{x}_t is a corruption of \mathbf{x}_0 . When t is small, \mathbf{x}_t retains high-correlation with \mathbf{x}_0 and therefore contains more information about \mathbf{x}_0 than the noisy measurement \mathbf{y} . In this regime, additional conditioning by \mathbf{y} contributes negligibly, and thus the approximation $\hat{\mathbf{x}}_{0|t,Y}(\mathbf{x}_t, \mathbf{y}) \approx \hat{\mathbf{x}}_{0|t}(\mathbf{x}_t)$ holds. Formalizing the above notion, we notice that

$$\hat{\mathbf{x}}_{0|t,Y}(\mathbf{x}_t, \mathbf{y}) \approx \hat{\mathbf{x}}_{0|t}(\mathbf{x}_t) - \eta \left(\frac{1 - \alpha_t}{\sqrt{\alpha_t}} \right) \|\mathbf{y} - \mathbf{A}\hat{\mathbf{x}}_{0|t}(\mathbf{x}_t)\|_2^2,$$

and $\alpha_t \rightarrow 1$ as $t \rightarrow 0$, we have that

$$\hat{\mathbf{x}}_{0|t,Y}(\mathbf{x}_t, \mathbf{y}) \approx \hat{\mathbf{x}}_{0|t}(\mathbf{x}_t) + o_t(1).$$

Empirically, we compared $\eta = 1$ and $\eta = 0$ in inference-time search algorithm using DPS as the gradient in the second term is computed by DPS, and found that $\eta > 0$ does not provide additional performance gains. Since the other base samplers (MPGD, DAPS) do not provide the term involving gradient, we use $\eta = 0$ for these methods.

Finally, we remark that since the base sampler guides towards \mathbf{y} explicitly from the likelihood term $\nabla_{\mathbf{x}_t} \log p_{t|Y}(\mathbf{x}_t)$, the generative process is gradually guided towards \mathbf{y} and therefore, we eventually sample from $p_{0|Y,S}$ (as suggested by Theorem 1) and *not just* $p_{0|S}$.

B.3 Algorithm

We summarize our framework in Algorithm 1. The GROUPSIZE step in line 5 computes the group-size at time t and can be changed to obtain various search strategies: Best-of-N, Greedy Search, and RFJ Search, and the RESAMPLE step in line 6 samples the indices within the groups as described in the main paper. Line 3 is specific to the diffusion samplers and how they implement it.

Here, we roughly explain how the entire algorithm is implemented in all the three diffusion samplers.

DPS: Compute the denoised mean and the clean data estimate $\boldsymbol{\mu}_t[i], \hat{\mathbf{x}}_{0|t}[i]$ from $\mathbf{x}_{t+1}[i]$. Compute $\mathbf{g}_t[i] = \nabla_{\mathbf{x}_t} \|\mathbf{y} - \mathbf{A}\hat{\mathbf{x}}_{0|t}(\mathbf{x}_{t+1}[i])\|_2^2$ and use it to update $\hat{\mathbf{x}}_{0|t,Y}[i] \leftarrow \hat{\mathbf{x}}_{0|t}[i] - \frac{1-\alpha_t}{\sqrt{\alpha_t}} \eta \mathbf{g}_t[i]$, and $\boldsymbol{\mu}_t[i] \leftarrow \boldsymbol{\mu}_t[i] - \zeta \mathbf{g}_t[i]$. Then, compute rewards based on $\hat{\mathbf{x}}_{0|t,Y}[i]$ to resample promising indices. Take the reverse diffusion step on the resampled $\boldsymbol{\mu}_t[I[i]]$ to obtain $\mathbf{x}_t[i]$.

DAPS: Compute the clean data estimate $\hat{\mathbf{x}}_{0|t}[i]$ from $\mathbf{x}_{t+1}[i]$. Compute the rewards based on $\hat{\mathbf{x}}_{0|t}[i]$, resample, and then take MCMC steps, starting from the resampled particles, to perform a local Langevin sampling [Zhang et al., 2025]. In the end, we obtain $\hat{\mathbf{x}}_{t,Y}[i]$, from which we sample $\mathbf{x}_t[i]$ by adding appropriate decoupled noise [Zhang et al., 2025].

MPGD: Compute the clean data estimate $\hat{\mathbf{x}}_{0|t}[i]$ from $\mathbf{x}_{t+1}[i]$. Compute gradient $\mathbf{g}_t = \nabla_{\mathbf{x}_{0|t}} \|\mathbf{y} - \mathbf{A}\hat{\mathbf{x}}_{0|t}[i]\|_2^2$. Take $\hat{\mathbf{x}}_{0|t,Y}[i] \leftarrow \hat{\mathbf{x}}_{0|t}[i] - \frac{1-\alpha_t}{\sqrt{\alpha_t}} \eta \mathbf{g}_t[i]$, and $\hat{\mathbf{x}}_{0|t}[i] \leftarrow \hat{\mathbf{x}}_{0|t}[i] - \zeta \mathbf{g}_t$. Resample indices based on rewards computed from $\hat{\mathbf{x}}_{0|t,Y}[i]$. Then, using the particles corresponding to the sampled indices $\hat{\mathbf{x}}_{0|t,Y}[I[i]]$, take a reverse DDIM step [He et al., 2024, Song et al., 2021a].

Algorithm 1 Inference-Time Search with Side Information for Inverse Problems

Require: Side information \mathbf{s} , observation \mathbf{y} , reward function r , resampling parameter B , number of particles N , temperature $\tau > 0$

- 1: Initialize N particles: $\mathbf{x}_T[i] \sim \mathcal{N}(0, \mathbf{I})$ for $1 \leq i \leq N$
- 2: **for** $t = T - 1$ to 0 **do**
- 3: Sample $\mathbf{x}_t[i] \sim p_{t|t+1, Y}(\cdot | \mathbf{x}_{t+1}[i], \mathbf{y})$, {Sample candidate particles}
- 4: $r[i] \leftarrow r(\hat{\mathbf{x}}_{0|t, Y}[i]; \mathbf{s})$ {Compute reward using side information}
- 5: $g_t \leftarrow \text{GROUPSIZE}(N, B, t)$ {Compute the group size at step t for resampling}
- 6: $I \leftarrow \text{RESAMPLE}(r, g_t, \tau)$ {Resample indices with replacement among the groups of size g_t }
- 7: $\mathbf{x}_t[i] \leftarrow \mathbf{x}_t[I[i]]$ {Retain the particles in the resampled indices}
- 8: **end for**
- 9: Select \mathbf{x}_0^* from $\hat{\mathbf{x}}_{0|0}[1 : N]$ (e.g., via reward maximization) and return \mathbf{x}_0^*

C Additional Experiments

C.1 Perceptual Improvements Do Not Guarantee Better PSNR/LPIPS/SSIM



Figure 8: Qualitative illustration of the relevance of the FaceSimilarity metric and the superior performance of RFJS in identity preservation. RFJS reconstruction is clearly more faithful to the ground truth, yet PSNR, SSIM, and LPIPS values slightly favor the BlindDPS outputs.

Perceptual improvements do not necessarily lead to better values in classical metrics such as PSNR, LPIPS, and SSIM. Figure 8 provides a clear qualitative example: it compares three samples generated by BlindDPS with our RFJS reconstruction. Visually, our method preserves identity much better, and this is reflected in a lower FaceSimilarity. However, all three BlindDPS reconstructions achieve better PSNR, LPIPS, and SSIM than our result, showing that these traditional metrics can fail to capture semantic improvements.

We provide further evidence in Figure 9, where our reconstructions are perceptually closer to the ground truth than those of DPS, especially in challenging $32\times$ super-resolution settings. For these examples, Table 5 reports the standard metrics for our method and for reconstructions under DPS. Once again, the perceptual gains visible in the images are not fully reflected in PSNR, LPIPS, or SSIM. This is important because the main goal in inverse problems is to recover the underlying *semantics* of the images, while PSNR, LPIPS, and SSIM are only proxies for reconstruction quality. When a metric better aligns with perceptual quality, it should be preferred. In our case, for face reconstruction this is captured by the FaceSimilarity metric, and for ImageNet settings by CLIPScore. In both cases, our method yields significant improvements over the baselines in these perceptual rewards.

This discrepancy is also intuitive from how these metrics are defined. PSNR is a purely pixel-level measure: it rewards putting the “right” colors in the “right” locations, even if the high-level content is not faithfully preserved. LPIPS and SSIM operate on features extracted by neural networks or on low-level structural patterns, and are more sensitive to capturing the correct class and coarse structure than to fine-grained semantics. For example, when reconstructing a human face, these metrics are not strongly incentivized to verify the correct identity; they mainly check that the output still looks like a plausible face. This explains why they may remain in the same range even when perceptual quality clearly improves.

We emphasize that marginal differences in PSNR, SSIM, and LPIPS between our method and the baselines should not be interpreted as a weakness of our approach. As demonstrated above, these

metrics are fundamentally misaligned with the goal of semantic reconstruction in ill-posed inverse problems, a conclusion supported by concurrent work [Lin et al., 2025, Su et al., 2025]. The relevant comparison is on task-specific perceptual metrics (FaceSimilarity and CLIPScore), where our method yields large and consistent improvements across all tasks and base samplers.

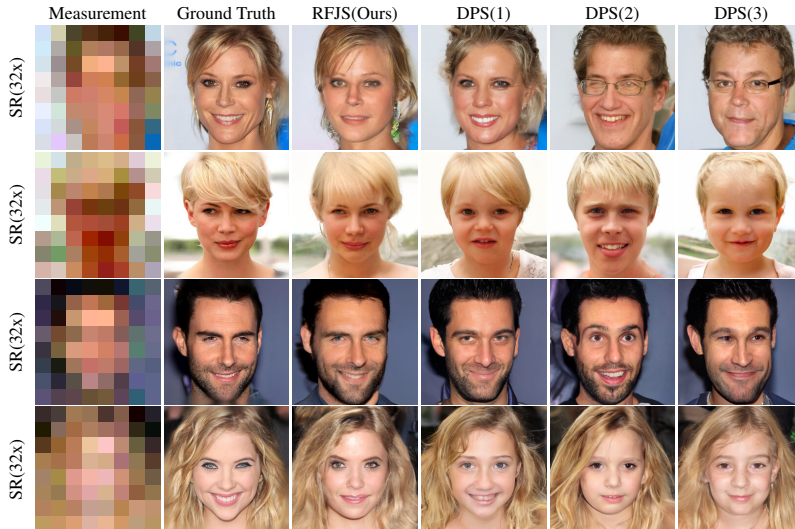


Figure 9: Our RFJS reconstructions preserve identity and perceptual details far better than DPS, as clearly visible from the images. This strong perceptual improvement is not reflected by classical metrics, which are reported in the table below.

Table 5: PSNR, LPIPS, and SSIM for the reconstructions shown in the figure above. Classical metrics fail to reflect the significant improvement.

Image ID	PSNR		LPIPS		SSIM	
	RFJS	DPS1	RFJS	DPS1	RFJS	DPS1
1	20.30	19.98	0.363	0.353	0.549	0.541
2	19.12	18.77	0.382	0.413	0.567	0.552
3	20.95	20.98	0.254	0.273	0.609	0.596
4	17.85	18.54	0.411	0.406	0.368	0.389
Avg	19.56	19.57	0.353	0.361	0.523	0.520

C.2 DPS

We also present additional qualitative examples for our DPS experiments in Figures 10 and 11, corresponding to settings that use face and text as side information, respectively.



Figure 10: Additional samples using DPS as the base sampler.

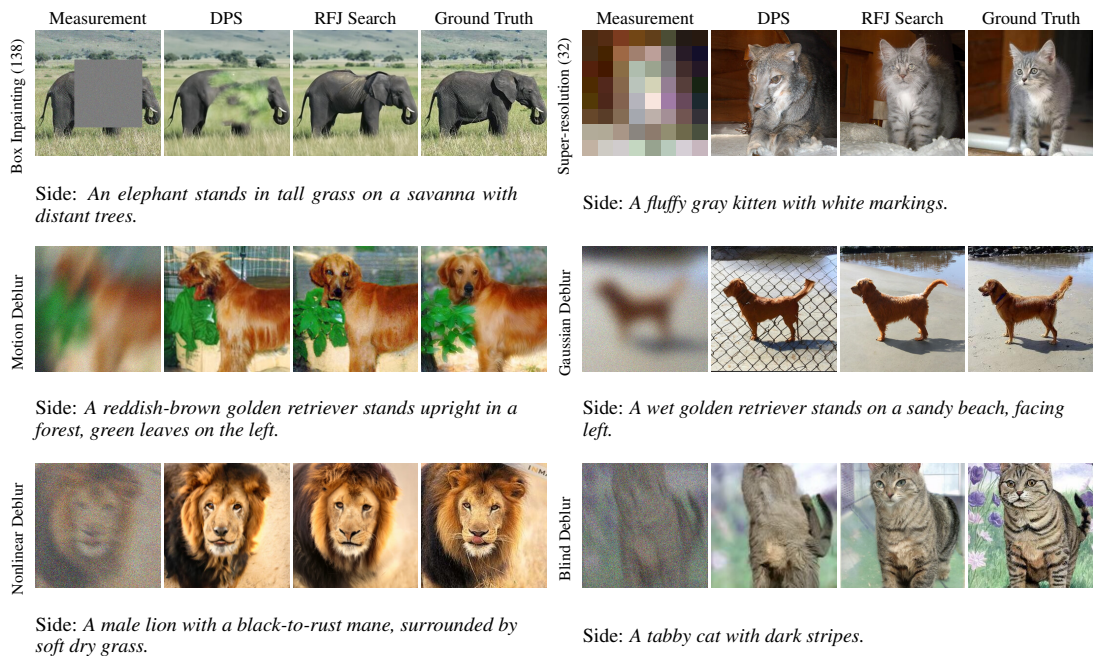


Figure 11: Qualitative comparison on ImageNet with textual side information. For highly degraded observations, DPS and BlindDPS often produce artifacts, whereas our method reduces these by better aligning reconstructions with the description.

C.3 DAPS

Setup: We employ the search and gradient modules to infuse side information using DAPS as the base sampler. We consider two challenging tasks, box inpainting with a box of size 96×96 and super-resolution with downsampling factor of 10. For gradient guidance, we used a scale of 15 with respect to the noise being added to $\hat{\mathbf{x}}_{0|t}(\mathbf{x}_t)$ after MCMC steps [Zhang et al., 2025]. DAPS uses fewer diffusion steps (200) than DPS (1000). Further, the algorithm is based on a graphical model that allows for more inherent exploration due to the decoupling between consecutive steps. Therefore, for search algorithms, relatively smaller bases are preferable, and hence $B = 4$ is chosen.

Results: The qualitative results are given in Figure 12, while the quantitative metrics are given in 6. Observe that for the task of inpainting, our search algorithm shows a significant improvement over DAPS, particularly in the FaceSimilarity metric.

Table 6: Comparison of metrics for various inverse problems using DAPS as the base sampler. For each metric, the best result is shown in **bold**, and the second best is underlined. We observe that our RFJ Search-based algorithm has the best or the second-best performance in all the tasks.

Method	Box Inpainting				Super Resolution ($\times 10$)			
	FaceSimilarity (\downarrow)	PSNR (\uparrow)	LPIPS (\downarrow)	SSIM (\uparrow)	FaceSimilarity (\downarrow)	PSNR (\uparrow)	LPIPS (\downarrow)	SSIM (\uparrow)
RFJS (ours)	0.423 ± 0.10	28.720 ± 1.35	0.140 ± 0.03	0.788 ± 0.03	<u>0.654</u> ± 0.11	<u>25.228</u> ± 1.34	0.282 ± 0.03	<u>0.661</u> ± 0.04
GS (ours)	0.511 ± 0.12	28.640 ± 1.43	<u>0.140</u> ± 0.03	<u>0.787</u> ± 0.03	0.760 ± 0.12	25.271 ± 1.36	0.285 ± 0.03	0.662 ± 0.04
RGG	<u>0.436</u> ± 0.12	28.410 ± 1.39	0.141 ± 0.03	0.784 ± 0.03	0.579 ± 0.13	25.210 ± 1.34	<u>0.282</u> ± 0.03	0.659 ± 0.04
BON	0.611 ± 0.14	<u>28.660</u> ± 1.45	0.141 ± 0.03	0.787 ± 0.03	0.909 ± 0.11	25.220 ± 1.38	0.285 ± 0.03	0.660 ± 0.04
DAPS	0.739 ± 0.18	28.290 ± 1.53	0.142 ± 0.03	0.784 ± 0.03	1.020 ± 0.14	25.170 ± 1.35	0.285 ± 0.03	0.659 ± 0.04



Figure 12: Qualitative comparison of algorithms using DAPS as the base sampler. Our method offers better reconstructions aligned with the identity.

C.4 MPGD

Setup: As in the paper He et al. [2024], we choose super-resolution and Gaussian deblurring as the tasks, along with additional task of box inpainting. For box inpainting, we used a box of size 64×64 at the center of the face. Further, we modified the down-sampling scale of super-resolution from 4 to 6, and the intensity of the kernel in Gaussian deblur from 3 to 5 to make the tasks more challenging. Even though MPGD uses 100 DDIM steps in generation, its exploratory capabilities are similar to DPS. Therefore, we cannot use very large base B , whence, we choose $B = 8$ for box inpainting, and super-resolution. For Gaussian deblur, we found that using $B = 8$ becomes detrimental for other metrics, and so $B = 16$ is used. For the gradient guidance, the scales of 0.5 for box inpainting, and 0.25 for super-resolution and Gaussian deblur are chosen carefully to avoid overfitting. This is the scale relative to the gradient with respect to the measurement. For more discussion and examples on the effect of gradient scale, see Appendix C.7.

Results: Experimental results with MPGD [He et al., 2024] as baseline algorithm are given in Table 7. We observe that using RFJ Search significantly enhances the FaceSimilarity (FS) metric, while improving the other metrics. The reconstructions that utilize the side information exhibit strong identity match with the ground truth, which is reflected in the FS metric.

Table 7: Quantitative comparison of reconstruction metrics in case of inverse problems with MPGD as the base sampler. For each metric, the best result is shown in **bold**, and the second best is underlined. Observe that our RFJ search algorithm has the best or the second-best performance in all the tasks. In Gaussian deblur, our search algorithm is only marginally worse than the best metrics attained. The value in the brackets indicates the resampling rate for search algorithms, and gradient scale for Gradient algorithm.

Sampler	Task	Method	FaceSimilarity (\downarrow)	PSNR (\uparrow)	LPIPS (\downarrow)	SSIM (\uparrow)
MPGD	Box Inpainting (64)	RFJS (8) (ours)	0.542 \pm 0.08	29.81 \pm 1.44	0.102 \pm 0.02	0.852 \pm 0.02
		GS (8) (ours)	<u>0.587</u> \pm 0.10	<u>29.44</u> \pm 1.75	<u>0.102</u> \pm 0.02	<u>0.851</u> \pm 0.02
		RGG (0.5)	0.609 \pm 0.08	29.24 \pm 1.30	0.103 \pm 0.02	0.850 \pm 0.02
		BON	0.661 \pm 0.08	29.35 \pm 1.82	0.102 \pm 0.02	0.851 \pm 0.02
		MPGD	0.766 \pm 0.07	29.09 \pm 1.27	0.103 \pm 0.02	0.848 \pm 0.02
	Super Resolution (6)	RFJS (8) (ours)	0.834 \pm 0.09	24.50 \pm 1.48	0.242 \pm 0.04	0.666 \pm 0.06
		GS (8) (ours)	0.878 \pm 0.08	<u>24.45</u> \pm 1.47	0.247 \pm 0.03	0.660 \pm 0.06
		RGG (0.25)	<u>0.854</u> \pm 0.07	24.39 \pm 1.44	0.246 \pm 0.03	0.656 \pm 0.05
		BON	0.964 \pm 0.09	24.44 \pm 1.58	<u>0.244</u> \pm 0.04	<u>0.664</u> \pm 0.06
		MPGD	1.037 \pm 0.07	24.39 \pm 1.45	0.249 \pm 0.03	0.657 \pm 0.06
	Gaussian Deblur (5)	RFJS (16) (ours)	<u>0.848</u> \pm 0.07	<u>24.19</u> \pm 1.40	0.229 \pm 0.03	<u>0.638</u> \pm 0.06
		GS (16) (ours)	0.893 \pm 0.07	24.14 \pm 1.39	<u>0.233</u> \pm 0.03	0.637 \pm 0.06
		RGG (0.25)	0.846 \pm 0.05	24.11 \pm 1.34	0.235 \pm 0.03	0.634 \pm 0.05
		BON	0.950 \pm 0.07	24.20 \pm 1.38	0.233 \pm 0.03	0.640 \pm 0.06
		MPGD	1.026 \pm 0.06	24.09 \pm 1.35	0.236 \pm 0.03	0.634 \pm 0.06



Figure 13: Qualitative comparison of algorithms using MPGD as the base sampler. Our method offers better reconstructions aligned with the identity. Notice that while the identity is preserved, the exact reconstruction might not be possible as witnessed in, for example, Box inpainting. The ground truth has a smiling face whereas the reconstruction does not, although being the same person. Thus, PSNR improvements over the base sampler might be small, but FaceSimilarity improvements are significant.

C.5 Stable Diffusion

To further demonstrate the generality of our framework, we evaluate it on Stable Diffusion, a large-scale latent diffusion model that natively conditions on text. A natural baseline in this setting is to simply pass the textual side information as the input prompt to Stable Diffusion and run the standard inverse problem solver (DAPS), which directly leverages the model’s native text-conditioning mechanism without any modification. We compare this baseline against our inference-time search applied on top of the same text-conditioned solver, where particles are selected using a reward that scores consistency between reconstructions and the textual side information.

Even though Stable Diffusion already incorporates the text prompt through its native conditioning, we find that performing inference-time search over the resulting trajectories yields further improvements. This indicates that text-conditioning alone does not fully exploit the information contained in the side description: search allows the solver to explore multiple plausible reconstructions consistent with the prompt and select those that best align with the side information through the reward.

We additionally compare against a Best-of- N variant that uses the same number of particles but selects the final reconstruction based on the measurement residual $\|\mathbf{y} - \mathbf{A}\mathbf{x}_0^i\|$ rather than the side-information reward. This measurement-based selection strategy fails to improve, and in noisy or severely ill-posed regimes can actively degrade, the reconstruction quality, since it favors particles that explain the noise rather than the underlying signal. In contrast, our reward-based selection using side information consistently improves all metrics across box inpainting, super-resolution, motion deblur, and Gaussian deblur tasks.

Qualitative reconstructions are shown in Figure 14, where our method recovers perceptually faithful content that aligns with the textual description, while the DAPS baseline often produces artifacts or content inconsistent with the prompt. Quantitative results are reported in Table 8, which confirms that selection by our reward $r(\mathbf{x}_0; \mathbf{s})$ yields consistent gains over both the base sampler and Best-of- N without side information. Together, these results show that our framework is complementary to native conditioning mechanisms and provides additional gains even when the base model is already trained to consume the same modality of side information.

	Box Inpainting				Gaussian Deblur			
Algorithm	PSNR (↑)	LPIPS (↓)	SSIM (↑)	CS (↑)	PSNR (↑)	LPIPS (↓)	SSIM (↑)	CS (↑)
BON (w/ SI, ours)	19.51	0.262	0.750	0.893	20.30	0.527	0.494	0.789
BON (w/o SI)	18.02	0.274	0.738	0.846	20.05	0.540	0.487	0.748
DAPS	18.21	0.274	0.742	0.855	19.86	0.540	0.481	0.735

	Super Resolution				Motion Deblur			
Algorithm	PSNR (↑)	LPIPS (↓)	SSIM (↑)	CS (↑)	PSNR (↑)	LPIPS (↓)	SSIM (↑)	CS (↑)
BON (w/ SI, ours)	18.65	0.579	0.398	0.767	19.54	0.551	0.474	0.770
BON (w/o SI)	18.13	0.590	0.368	0.729	18.18	0.562	0.462	0.718
DAPS	18.44	0.583	0.391	0.727	19.49	0.556	0.466	0.722

Table 8: Without side information, Best-of- N selection by $\|\mathbf{y} - \mathbf{A}\mathbf{x}_0^i\|$ fails to improve over the baseline and can degrade it. With side information, selection by our reward $r(\mathbf{x}_0; \mathbf{s})$ consistently improves all metrics (Box Inpainting and Super Resolution are reproduced from the table provided in the section Role of side information in the main paper).

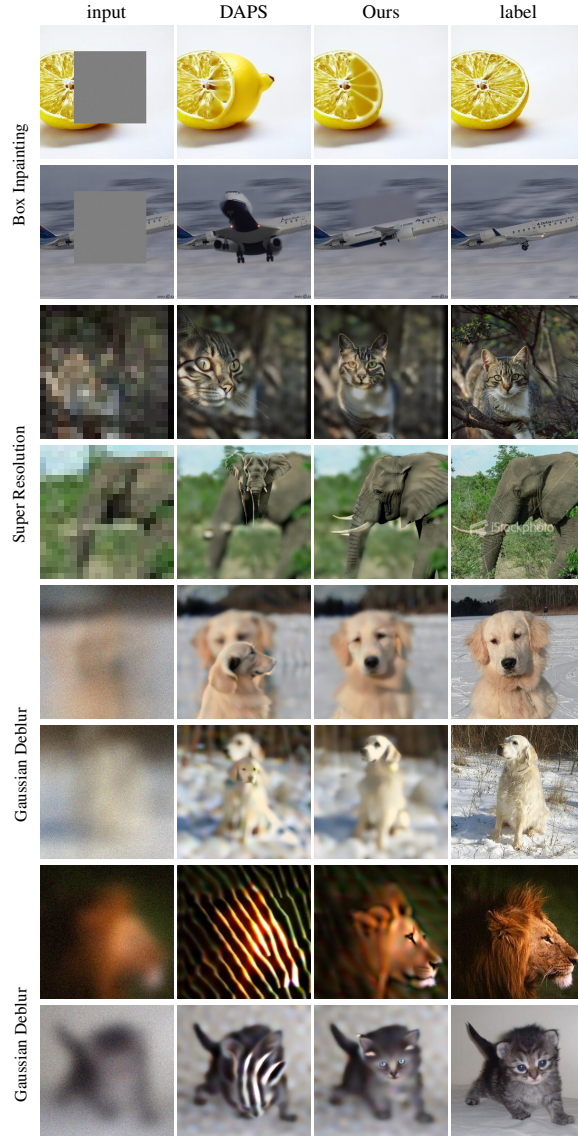


Figure 14: Stable Diffusion

C.6 Ablation Studies

In this section, we conduct ablation studies to study the performance and robustness of our algorithm by degrading: (i) Measurement quality and (ii) Side information quality.

C.6.1 Measurement Quality: Hard Inverse Problems

In this section, we demonstrate the effectiveness of our method on hard inverse problems with severely degraded measurements. For DPS, we evaluate inpainting with a large mask that covers almost the entire face, super-resolution with aggressive downsampling ratios of $12\times$ and $32\times$, and motion deblurring using a large 256-pixel kernel. For MPGD, we similarly consider challenging variants of inpainting, super-resolution, and Gaussian deblurring, with quantitative results reported in Tables 9 and 10. Across all settings, our method consistently improves the target reward metric, which translates directly into stronger qualitative performance, and we also observe improvements in classical metrics on average. The qualitative results are shown in Figures 15, 16, 9. For textual side information, we already include challenging experimental settings in the main paper; see Figure 5 and Table 3.

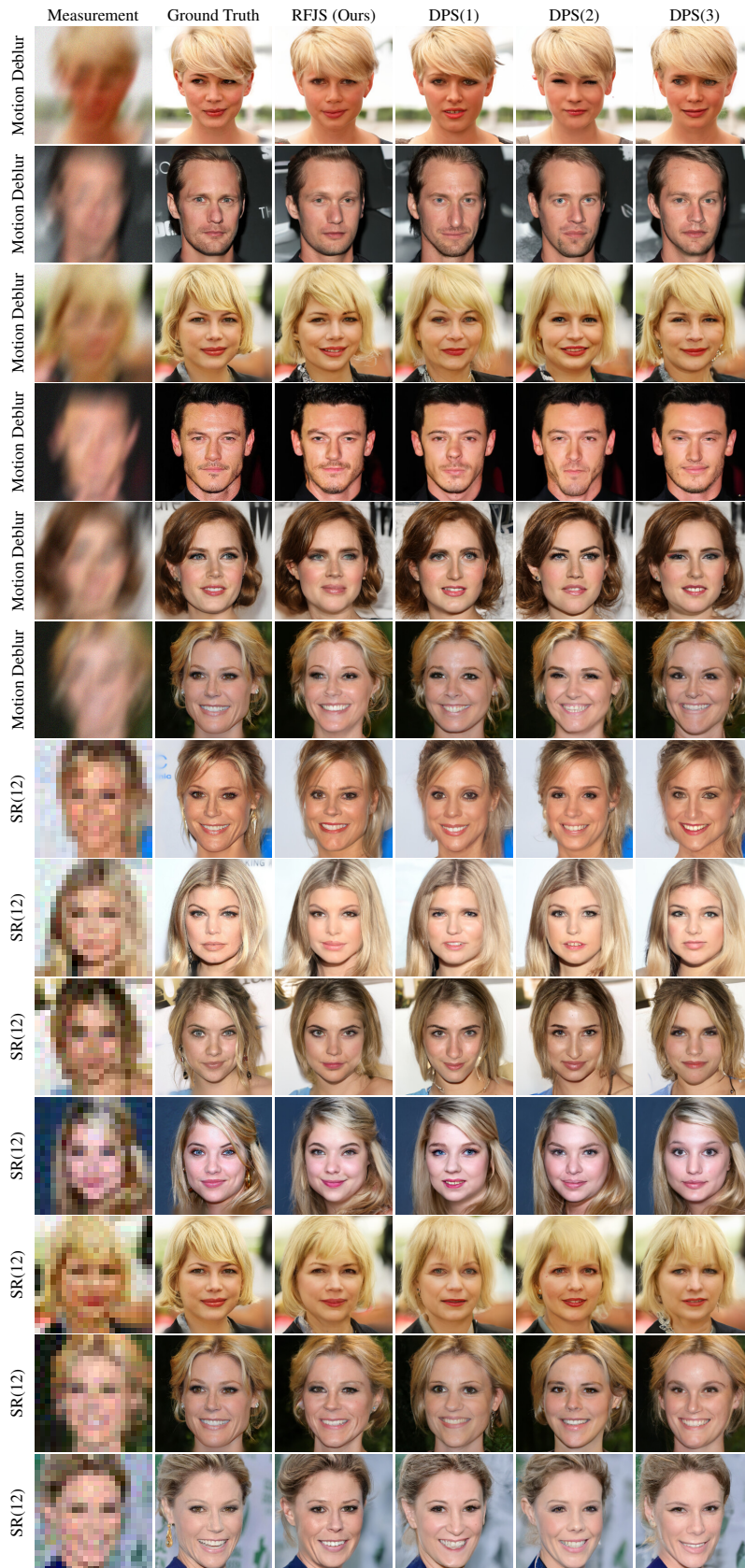


Figure 15: Qualitative results on hard tasks using DPS. Our algorithms reconstructs faces with perceptual quality.

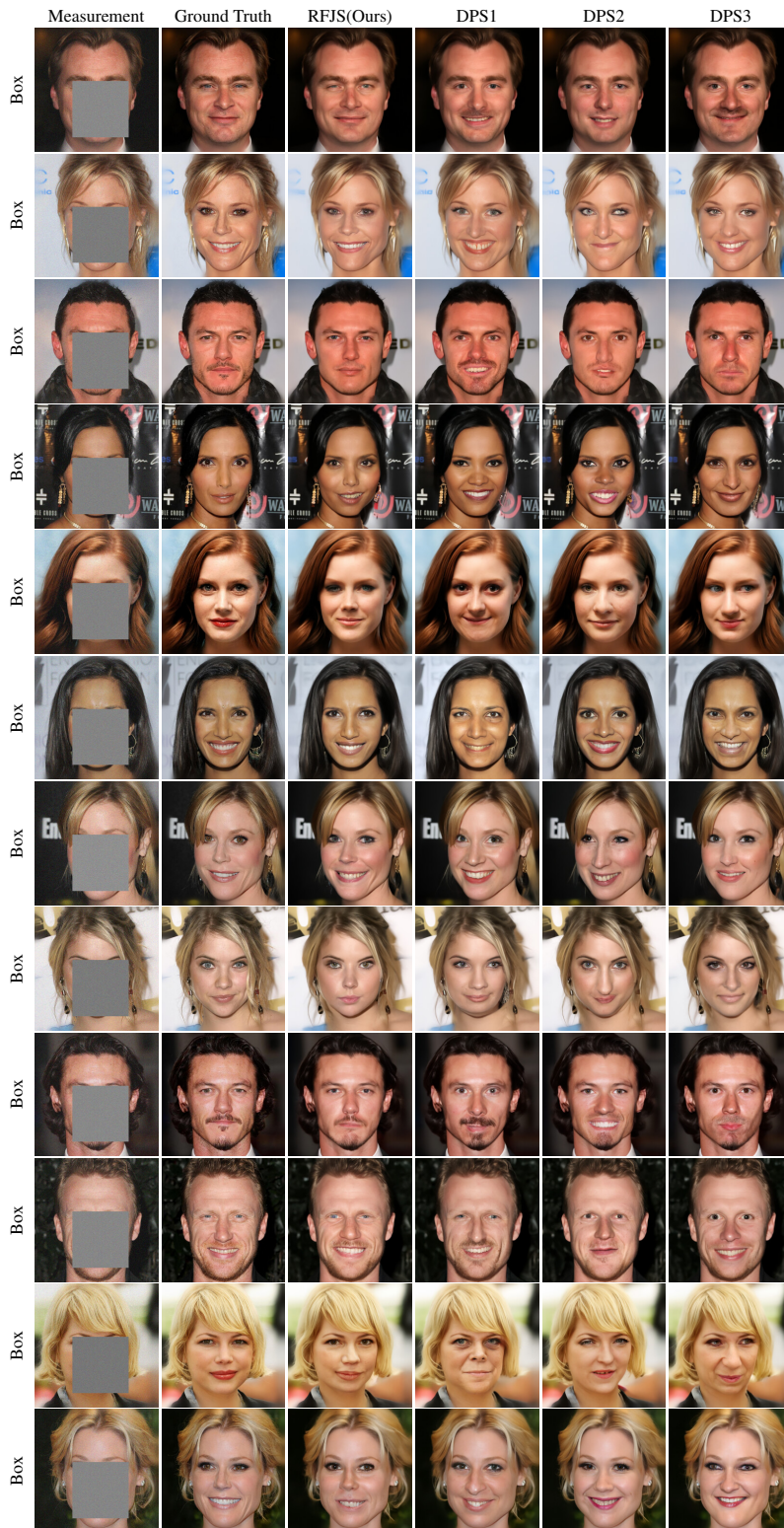


Figure 16: Qualitative results on box inpainting using DPS sampler. Since the face is completely masked in the measurement, side information provides useful clues so that the reconstruction preserves identity.

Table 9: Quantitative results using DPS for hard tasks with dps scale = 0.8 (guidance strength from the measurement y)

Task Name	Task Parameters	Algo	FS (\downarrow)	PSNR (\uparrow)	LPIPS (\downarrow)	SSIM (\uparrow)
Box Inpainting	$M = 116$	RFJS	0.47	26.62	0.140	0.839
		DPS	1.07	26.21	0.151	0.826
Super Resolution	$S = 12$	RFJS	0.603	22.92	0.262	0.619
		DPS	1.23	22.78	0.265	0.613
	$S = 32$	RFJS	0.748	18.66	0.354	0.496
		DPS	1.38	18.43	0.363	0.489
Motion Deblur	$K = 256$	RFJS	0.545	22.67	0.257	0.614
		DPS	1.21	22.69	0.260	0.615

Table 10: Quantitative results using MPGD for hard tasks with scale = 6.0 (guidance strength from the measurement y)

Task Name	Task Parameters	Algo	FS (\downarrow)	PSNR (\uparrow)	LPIPS (\downarrow)	SSIM (\uparrow)
Inpainting	$M = 96$	RFJS	0.594	24.83	0.171	0.749
		MPGD	0.831	24.79	0.172	0.747
Super Resolution	$S = 12$	RFJS	1.032	21.40	0.312	0.555
		MPGD	1.282	21.32	0.318	0.553
	$S = 16$	RFJS	1.142	19.03	0.383	0.486
		MPGD	1.356	19.01	0.381	0.486
Gaussian Deblur	$K = 81, I = 5.0$	RFJS	0.820	24.49	0.238	0.645
		MPGD	0.993	24.39	0.241	0.641

C.6.2 Side Information Quality

In this subsection, we evaluate how the quality of side information affects the performance of our method. For the face experiments, we study a $4\times$ super-resolution task using DPS as the base sampler. We degrade the side information by applying a Gaussian blur with a 31×31 kernel and varying blur intensities. Figure 17 reports the resulting Face Similarity scores. As expected, performance consistently improves as the side information becomes more reliable. The case with blur intensity 0.0 corresponds to the unaltered side information and matches the results reported in the main paper. Representative qualitative examples are provided in Figure 18. Notably, even with heavily degraded side information (intensity 5.0), our method (FS: 0.53) outperforms the baseline (FS: 1.042), and the performance steadily improves as the fidelity of the side information increases.

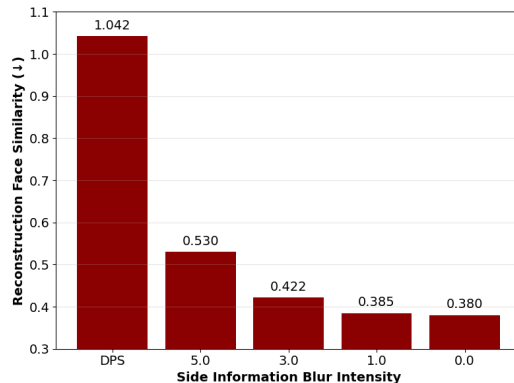


Figure 17: Performance of RFJS algorithm with side information blurred with Gaussian kernel in the face data experiments

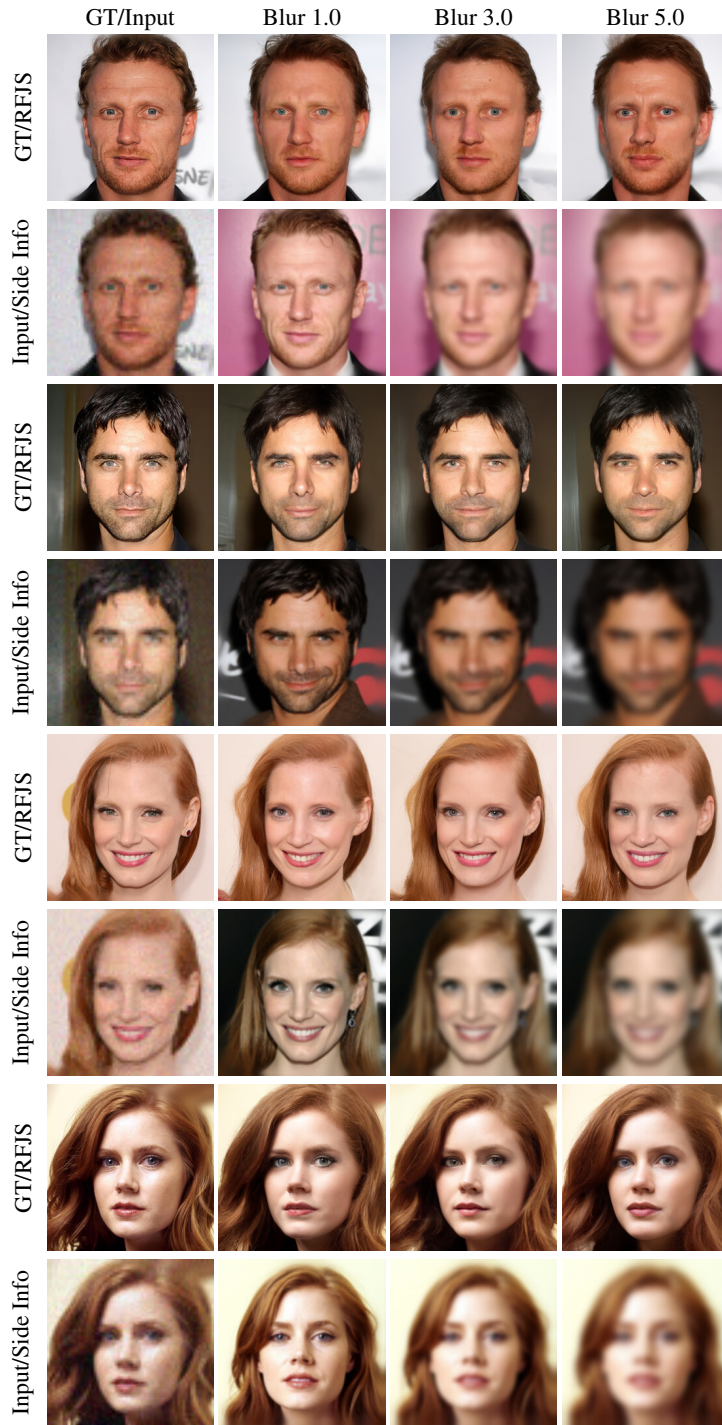


Figure 18: Qualitative comparison of generations with side information blurred at different levels. Some sharp features that preserve identity are lost when the side information is severely blurred. In the last three columns, first rows indicate reconstruction and second rows indicate the blurred side information that is used to guide the generation process.

For the case of textual side information, Figure 19 shows that our method remains consistent under small variations in the prompt. In this example, the key missing information in the measurement is the type of animal or object present in the scene. Once the side information specifies that there is a golden retriever, the reconstruction improves significantly. Further modifying the prompt does not

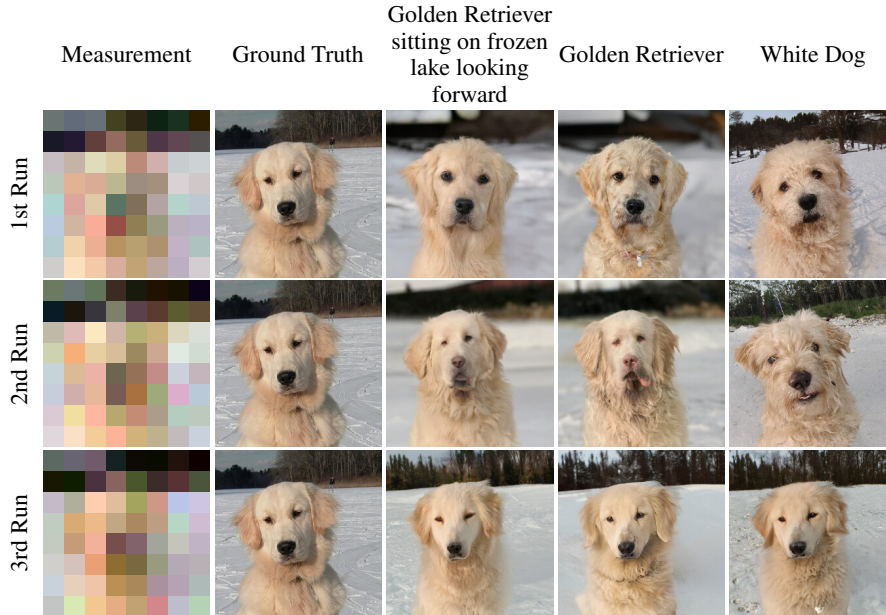


Figure 19: Qualitative comparison of generations with different textual descriptions as side information. Due to randomness and robustness of the algorithm due to relative ordering, the quality assessment is difficult.

substantially affect the output. If the side information is "white dog", then our algorithm reconstructs a dog which is not necessarily a golden retriever (Figure 19, last column).

C.7 Experiments on Effect of Gradient Scale

Gradient Guidance Limitations. While guiding the reverse diffusion process with reward gradients can help generate images with higher reward scores, this approach has several limitations. First, as shown in Figures 20, 21, gradient-based guidance primarily adds fine details, such as wrinkles or texture, to the reconstruction, but it cannot significantly alter the global structure of the face. To isolate the effect of the gradient, we used fixed noise realizations for both the gradient-based and baseline methods. The results show that changes are mostly confined to local details, implying that if the sampling trajectory is poor, gradient guidance alone cannot compensate. This highlights the need for search-based methods that can explore a wider range of trajectories during inference.

Second, this method is sensitive to the choice of gradient scale. In the visual examples, we used a relatively large scale of 1.6 to make the gradient’s effect more visible; however, such high scales often degrade other metrics like PSNR and SSIM and introduce artifacts. Empirically, we found that a scale around 0.5 yields the best balance when the base sampler is DPS or BlindDPS, consistently improving the FaceSimilarity metric while preserving other evaluation metrics and avoiding artifacts (see Figure 21). Moreover, the sensitivity to gradient scale increases when the number of reverse diffusion steps is small. For instance, in DAPS (Figure 20) and MPGD, where the number of steps is limited to 200 and 100 respectively, larger scales quickly lead to visible artifacts, as demonstrated in Figures 22, and 23.

It is well established in deep learning research that deep (convolutional) neural networks are vulnerable to gradient-based adversarial attacks [Goodfellow et al., 2015]. Consequently, using such networks to provide reward-based guidance inherits these vulnerabilities. However, when combined with diffusion samplers, this susceptibility is partially alleviated, as the diffusion process can help steer trajectories away from adversarially induced local minima. This mitigating effect is particularly evident when using a large number of sampling steps (e.g., 1000 steps in DPS). In contrast, samplers with fewer steps (e.g., 100 steps in MPGD) exhibit increased sensitivity to the gradient scale, as illustrated in Figures 22 and 23.



Figure 20: **Effect of reward-gradient guidance in diffusion-based inverse problems.** We show 4 runs with different random seeds (rows), and for each seed we vary the gradient scale across 4 settings (columns). Within each row, the noise realization is identical and only the gradient scale changes; within each column, the gradient scale is fixed while the random seed varies. The ground truth and degraded input are the same for all reconstructions. This arrangement reveals two key observations: (1) The reward gradient influences fine details, such as wrinkles and facial lines without altering the overall facial structure; the structure is primarily determined by the initial noise realization. (2) Different seeds reconstruct different face structures, highlighting the multi-modal nature of the problem. This demonstrates why using multiple particles and performing search across them is beneficial: it enables exploration of structurally different hypotheses while the reward gradient refines locally.

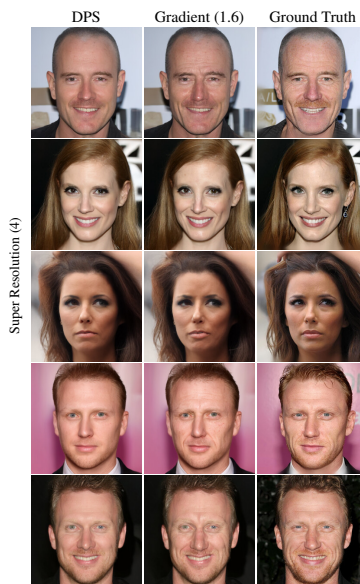


Figure 21: Qualitative comparison of the effect of gradient scale on reconstruction paths.



Figure 22: Qualitative comparison of the effect of gradient scale on reconstruction paths. Notice that while the base reconstruction is reasonable, adding the gradient can degrade it if the scale is very large. The final scale used in the experiments is 0.5.

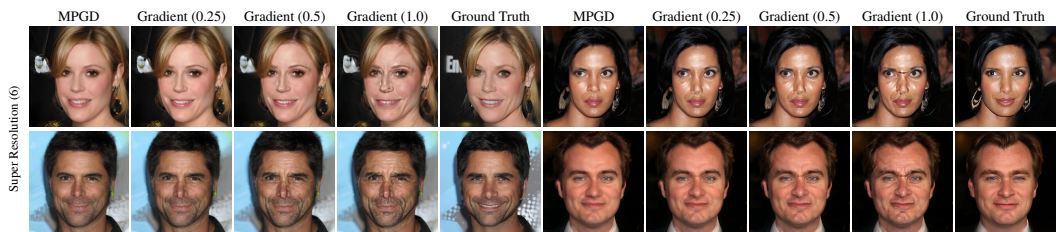


Figure 23: Qualitative comparison of the effect of gradient scale on reconstruction paths for super resolution task. Notice that while the base reconstruction is reasonable, adding the gradient can degrade it if the scale is very large. The final scale used in the experiments is 0.25.

C.8 Effect of Number of Particles

In this section, we study how performance scales with the number of particles. Figure 24 presents the results for the box inpainting task using RFJS with DPS as the baseline sampler, while Figure 25 reports the corresponding results for the remaining tasks. The evaluations using MPGD as the baseline are shown in Figure 26. Across all tasks and for both baseline samplers, we observe a consistent improvement in performance as the number of particles N increases, aligning with the expected behavior of particle-based search methods. Furthermore, our results indicate that RFJS scales more efficiently with increasing N than both Greedy Search and Best-of-N.

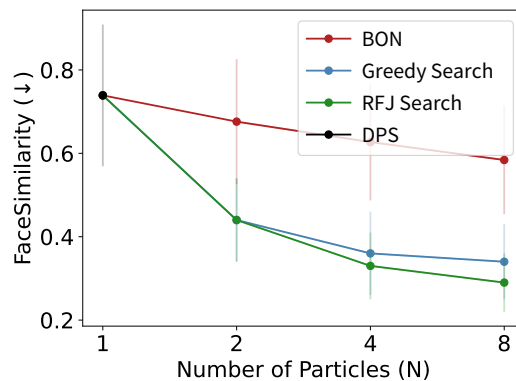


Figure 24: Scaling of search algorithms with respect to the number of particles.

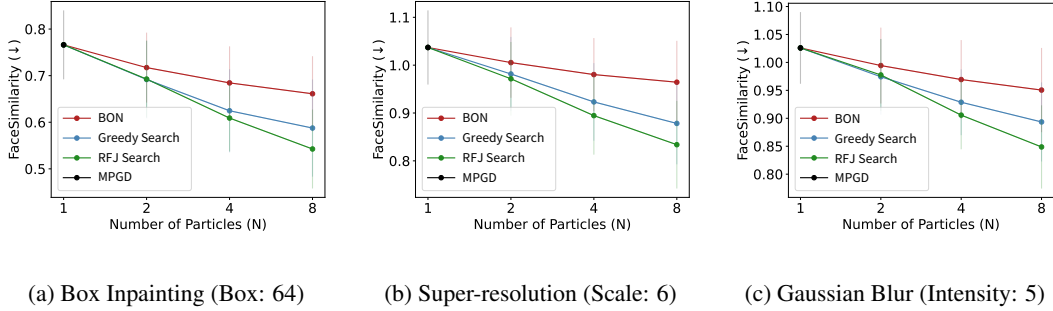


Figure 26: Effect of number of particles N on the FaceSimilarity metric. RFJ Search algorithm offers the best scaling performance, followed by Greedy Search algorithm. Finally, BestOfN performance improves, but only marginally. 64 indicates the size of the box for inpainting, 6 indicates the down-sampling factor in super-resolution, and 5 is the intensity of the Gaussian kernel in Gaussian deblur.

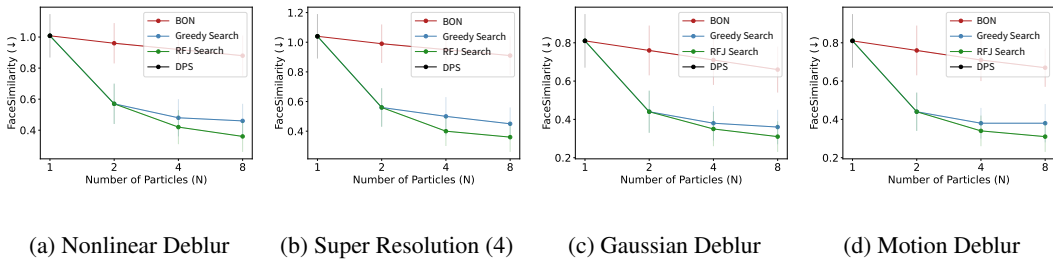


Figure 25: Effect of the number of particles N on the FaceSimilarity metric in DPS. As N increases, the performance improves.

C.9 Runtimes

Table 11 reports wall-clock runtimes (in seconds) for our search algorithms compared to Best-of-N (BON) and Greedy Search across different baselines (DPS, DAPS, and MPGD) with varying numbers of particles. When the number of particles is set to 1, the runtime corresponds to the baseline method without search. As the number of particles increases, amount of computation scales linearly with N , but thanks to parallelization, the wall-clock overhead remains moderate: with $N = 8$, runtimes are only $4 - 5 \times$ those of the baseline. We also note that our RFJ Search method take slightly more time than BON and Greedy Search, but consistently achieve better reconstruction quality, highlighting the practical efficiency of our approach.

Finally, resampling of the particles requires computing the rewards, which involves call to the reward evaluation model. Therefore, decreasing the base B (more frequent resampling) increases the wall-clock time. Denoting c_d, c_r the computation cost per function call to diffusion model and reward model respectively, a rough estimate of the time taken to run the algorithm is given by:

$$N(O(Tc_d) + O((T/B)c_r)) \leq N(O(Tc_d) + O(Tc_r)),$$

where T denotes the number of diffusion steps and N the number of particles. However, it is important to note that the wall-clock time is dominated by the call to the diffusion model, which is a much larger network than the reward model, i.e. $c_d \gg c_r$ in practice, and so the reward evaluation does not add a significant overhead.

The compute-quality tradeoff is a feature, not a limitation. Our framework provides a controllable knob: increasing N yields better reconstructions, while $N = 1$ recovers the base sampler exactly at no additional cost. This is precisely the inference-time scaling behavior that has driven recent progress in LLMs [Snell et al., 2025, Setlur et al., 2025], and is a desirable property rather than a drawback. We also note that any additional runtime cost is *inherent to inference-time search as a paradigm*, it is not specific to our method. BON, Greedy Search, and any other particle-based approach share the same linear scaling with N . What distinguishes our framework is that the added

compute is spent meaningfully: as shown in Fig. 1 (right), scaling N without side information yields negligible gains, whereas our reward-guided search produces consistent and significant improvements with every additional particle. **The runtime cost is therefore justified by gains that no amount of unguided compute scaling can achieve.**

Table 11: Runtime (seconds) vs number of particles for BON, Greedy Search, and RFJ Search methods on DPS, DAPS and MPGD ($B = 8$). The baseline algorithm corresponds to $N = 1$.

Particles	BON	Greedy Search	RFJ Search	Particles	BON	Greedy Search	RFJS	Particles	BON	Greedy Search	RFJS
1	55	-	-	1	61	-	-	1	3	-	-
2	65	75	75	2	72	91	91	2	4	5	5
4	102	118	131	4	125	141	157	4	5	8	9
8	180	195	241	8	229	245	290	8	8	12	23

(a) Task: Box inpainting. Baseline: DPS

(b) Task: Box inpainting. Baseline: DAPS

(c) Task: Box inpainting. Baseline: MPGD

C.10 Ablation on Reward Function

Choice of reward function. A natural question is how to choose the reward function $r(x_0; s)$ and how sensitive the framework is to this choice. As discussed in Section 4.1, the reward function need only satisfy a simple and intuitive condition: it should assign high values to pairs (x_0, s) that are consistent, and low values to inconsistent pairs. Any pretrained model that captures this notion of pairwise consistency is a valid candidate. In practice, such models are widely available for common side-information modalities, face recognition networks for image side information, and text-image alignment models for textual side information, and require no additional training.

To identify the best candidate for each modality, we conducted a brief literature review of pretrained models known to capture the relevant notion of consistency in prior recognition or generative modeling settings. For face side information, we evaluated AdaFace Kim et al. [2022] and FaceNet, both trained to assign higher similarity to image pairs from the same identity. For textual side information, we evaluated ImageReward Xu et al. [2023] and CLIP score Radford et al. [2021], where the former is trained to reflect human preference and text-image alignment, and the latter uses a contrastive objective for matched image-text pairs.

We note that during diffusion sampling, the reward is evaluated on intermediate denoised estimates $\hat{x}_{0|t}(x_t)$ (the Tweedie estimate) rather than directly on the noisy state x_t , since $\hat{x}_{0|t}$ lies closer to the image manifold and therefore falls more reliably within the distribution on which these networks were trained. Robustness to such intermediate inputs was an additional practical consideration in our selection.

Crucially, *all reward candidates we tested improved over the baseline*, confirming that the framework is not sensitive to the specific choice of reward, as long as it satisfies the consistency condition above. We ultimately selected AdaFace and ImageReward as they yielded the strongest empirical performance. The full comparison is reported in Tables 12 and 13.

Clarification on optimization target vs. evaluation metric. We wish to explicitly address a potential source of confusion. Our method optimizes the reward $r(\hat{x}_0; s)$, which measures consistency between the *reconstructed image* \hat{x}_0 and the *side information* s . However, the FaceSimilarity (FS) metric reported in our tables measures the distance between the *reconstructed image* \hat{x}_0 and the *ground truth* x_0^* .

These are **not the same quantity**. The ground truth x_0^* is never observed at inference time and plays no role in the reward computation or the search procedure. The side information s is a *different* image of the same identity, taken under different conditions (pose, lighting, etc.), and is not equal to x_0^* . So the improvements we get are not a consequence of optimizing the same quantity that is being measured, and it is not reward hacking.

Below, we provide an ablation on choice of reward functions for face as side information and text as side information.

Task	Param	Algo	FS↓	PSNR↑	LPIPS↓	SSIM↑
Box Inpainting	$M=96$	DPS	0.739	<u>27.93</u>	0.139	0.852
		FaceNet	<u>0.534</u>	26.55	0.144	<u>0.852</u>
		AdaFace	0.308	28.29	0.136	0.855
Super Resolution	$S=12$	DPS	1.23	<u>22.78</u>	0.265	<u>0.613</u>
		FaceNet	<u>0.962</u>	22.69	<u>0.265</u>	0.608
		AdaFace	0.603	22.92	0.262	0.619
Motion Deblur	$K=256$	DPS	1.21	22.69	0.260	0.615
		FaceNet	<u>0.945</u>	21.88	0.277	0.587
		AdaFace	0.545	<u>22.67</u>	0.257	<u>0.614</u>

Table 12: Comparison of RFJS with different reward functions for image side information. FaceSimilarity (FS) is evaluated against the *ground truth* (not the side information used during inference). Both FaceNet and AdaFace improve over the DPS baseline, confirming that any reward satisfying the consistency condition is beneficial; AdaFace achieves the best overall performance and is used in the main paper.

Task	Param	Algo	CS↑	PSNR↑	LPIPS↓	SSIM↑
Box Inpainting	$M=138$	DPS	0.866	19.87	0.314	0.667
		CLIP	<u>0.875</u>	<u>19.93</u>	<u>0.305</u>	<u>0.670</u>
		ImageReward	0.895	20.75	0.290	0.681
Super Resolution	$S=32$	DPS	0.737	<u>16.83</u>	0.521	<u>0.326</u>
		CLIP	<u>0.784</u>	16.37	<u>0.511</u>	0.311
		ImageReward	0.814	17.10	0.493	0.343
Motion Deblur	$K=256$	DPS	0.783	<u>17.70</u>	0.468	<u>0.364</u>
		CLIP	<u>0.836</u>	17.60	<u>0.465</u>	0.353
		ImageReward	0.866	18.27	0.439	0.367

Table 13: Comparison of RFJS with different reward functions for textual side information. CLIP-Score is evaluated against the *ground truth* image (not the text prompt used during inference). Both CLIP-based and ImageReward-based rewards improve over the DPS baseline; ImageReward achieves the best performance and is used in the main paper.

C.11 Hyperparameter Sensitivity

Our framework introduces very few hyperparameters. The temperature τ controls the softness of particle resampling, but as discussed in Section 4.2, RFJS naturally balances exploration and exploitation through its hierarchical grouping structure, because of this, in practice, we set τ to a sufficiently small value so that resampling becomes deterministic (always retaining the highest-reward particle within each group), eliminating τ as a tuning parameter entirely.

The primary remaining hyperparameter is the resampling base B . We conduct an ablation study over $B \in \{4, 8, 16, 32\}$ on the box inpainting task using DPS as the base sampler, with $N = 8$ particles. The results are reported in Table 14. Across all values of B , RFJS substantially improves the perceptual FaceSimilarity (FS) metric over the DPS baseline (from 0.739 to a range of 0.296–0.434), while keeping classical metrics (PSNR, LPIPS, SSIM) in a consistently better range. Crucially, the variation across choices of B is small, confirming that the method is not sensitive to this hyperparameter.

In practice, we select B once per base sampler, reflecting properties of the sampler such as its number of diffusion steps and degree of inherent exploration, and apply the same value uniformly across all tasks using that sampler. No per-task tuning of B is performed.

Method	PSNR \uparrow	LPIPS \downarrow	SSIM \uparrow	FS \downarrow
DPS (baseline)	27.929	0.1391	0.8519	0.739
RFJS ($B=4$)	<u>28.360</u>	0.1365	0.8562	0.296
RFJS ($B=8$)	28.186	0.1354	0.8551	<u>0.330</u>
RFJS ($B=16$)	28.385	<u>0.1363</u>	0.8562	0.372
RFJS ($B=32$)	28.264	0.1383	<u>0.8553</u>	0.434

Table 14: Ablation over resampling base B for RFJS with DPS on box inpainting ($N=8$, $M=96$). All values of B substantially improve the perceptual FaceSimilarity (FS) metric over the DPS baseline, and classical metrics remain in a consistently better range across all choices, demonstrating low sensitivity to B .

C.12 Evaluating Search Strategies in a 2D Setting

To illustrate the effect of side information in inference-time search, we consider a simple 2D setup. The prior on x_0 is a mixture of Gaussians, shown in the leftmost image of Figure 28. A ground-truth sample x_0 is drawn from this prior, and a random forward operator A is generated with fixed norm and random orientation. The observation is then $y = Ax_0 + n$. The corresponding posterior $p(x_0 | y)$, approximated by DPS, is also shown in Figure 28. Because this is an ill-posed inverse problem, the posterior is multimodal and DPS fails to reconstruct the correct solution.

We then add side information of the form $s = Dx_0 + n_s$, where D is chosen so that Dx_0 is orthogonal to Ax_0 . The reward function is defined as $r(x_t, s) = -\|s - D\hat{x}_0(x_t)\|_2^2$, where $\hat{x}_0(x_t)$ is the Tweedie estimate of the clean signal from the noisy state x_t . Using this reward, RFJ Search produces posterior samples $p(x_0 | y, s)$ as shown in the three rightmost images of Figure 28. As the resampling base B decreases, the particles concentrate more tightly around the ground truth, highlighting how side information guides inference.

To compare RFJ and Greedy Search, we next consider a more realistic scenario where side information is generated through a neural network reward model. For example, in face reconstruction tasks, side information may come from the embedding of an additional image, while for text-conditioned tasks, it may come from a text encoder. To mimic this, in each trial we sample a ground truth x_0 , a forward operator A , and a reward network r_θ with randomly initialized weights. The side information is defined as $s = r_\theta(x_0) + n_s$, and the reward is the cosine similarity between $r_\theta(\hat{x}_0(x_t))$ and s . We repeat this experiment 16,000 times, and for each trial run both RFJ and Greedy Search 128 times with $N = 8$ particles, varying the resampling base B over powers of two from 1 to 256. The average PSNR values are reported in Figure 27. Across all settings, RFJ Search consistently outperforms Greedy Search, with the best performance observed at $B = 4$.

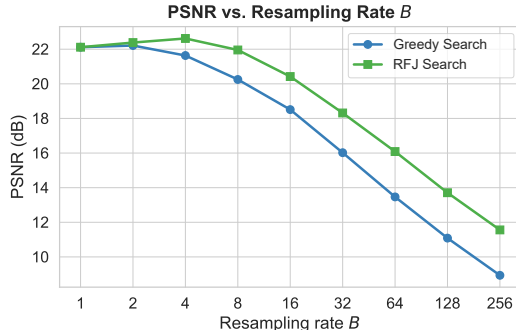


Figure 27: Comparison of performance of RFJ Search (RFJS) and Greedy Search (GS) as a function of B for a randomly generated reward network r_θ . RFJS outperforms GS across all values of B .

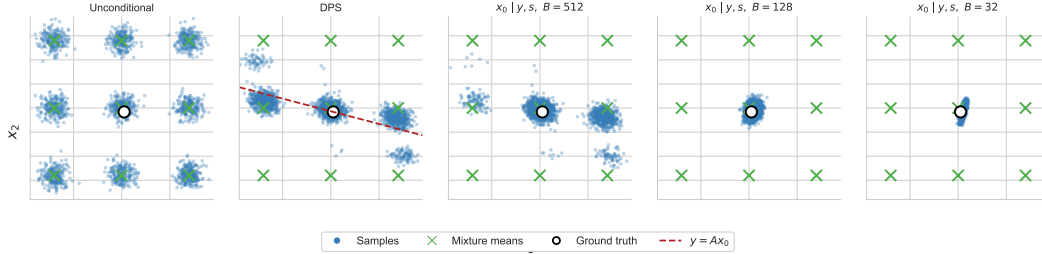


Figure 28: Illustration of the effect of B in utilization of side information for the reconstruction in a linear inverse problem with a mixture of Gaussian prior.

D Hyperparameters

In our implementation of RESAMPLE in Algorithm 1, we perform a greedy resampling, i.e., we pick the best candidate within each group of size g_t and replicate it g_t times. Since we are using large enough B , this is justified and has similar effect as using smaller B with moderate temperature, with the added advantage of utilizing less function calls to the reward network r . Thus, tuning the B allows us to maintain balance without over-optimizing with respect to the reward.

For reproducibility, we provide detailed settings for each task, sampler, and search algorithm used in our experiments below.

D.1 Face Identity Experiments

For experiments with face identity as side information:

- **DPS:** Box inpainting with box size 96. All other parameters (downsampling rate, blur kernel, noise levels) are the same as the default DPS settings in the implementation. Search algorithms use $N = 8$ particles and resampling base $B = 16$ for both RFJ and Greedy search. Gradient guidance is applied with scale 0.5.
- **DAPS:** Box inpainting with box size 96, super-resolution with downsampling rate $10\times$. Noise levels unchanged from original DAPS defaults. Search algorithms use $N = 8$ particles and resampling base $B = 4$, with gradient guidance scale 13.
- **MPGD:** Box inpainting with box size 64, super-resolution with downsampling rate $6\times$, and Gaussian deblur with intensity of 5.0. Search algorithms use $N = 8$ particles and resampling base $B = 8$. Gradient guidance scale is 0.5 for box inpainting and 0.25 for super-resolution and Gaussian deblur.

D.2 Text Side Information Experiments

When text descriptions were used as side information, we made the degradation more severe so that the information in s was not already present in the measurement y . Otherwise, side information would not provide meaningful guidance. For example, if the input image is sharp enough to identify the type of animal, then explicitly stating it in s adds little value.

The settings for these tasks are:

- **Box inpainting:** Box size 138, noise level same as default.
- **Super-resolution:** Downsampling rate $32\times$, noise level same as default.
- **Motion/Gaussian deblur:** Kernel size 256, intensity of Gaussian 5.0, noise level 0.1.
- **Nonlinear/Blind deblur:** Kernel size unchanged, noise level 0.5.

For all tasks in this setting, search algorithms use $N = 4$ particles and resampling base $B = 100$.

These hyperparameters ensure that our framework is evaluated under severe degradations (heavy downsampling, blurring, or noise), while search and guidance settings remain consistent across samplers and modalities.

Table 15: Quantitative MRI reconstruction results (fastMRI knee, AF=16, ACS=2%).

PDFS with PD				
Algorithm	PSNR (\uparrow)	SSIM (\uparrow)	LPIPS (\downarrow)	NMI (\uparrow)
RFJS	25.85	0.801	0.375	0.457
GS	25.33	0.797	0.375	0.455
BON	25.47	0.797	0.376	0.454
ContextMRI	25.39	0.795	0.383	0.451
PD with PDFS				
RFJS	27.85	0.920	0.358	0.579
GS	27.80	0.920	0.360	0.579
BON	27.80	0.918	0.366	0.570
ContextMRI	27.46	0.915	0.375	0.563

D.3 MRI Experiments

We used the contrast-pairings among the files in the fastMRI dataset, provided by Atalik et al. [2025]. We collect the data from the (fastMRI) source and preprocess to be compatible with the inputs in ContextMRI. Specifically, the setup used in the data is multi-coil MRI acquisition, which requires us to estimate the coil sensitivity maps, and then a complex reconstruction from them. ContextMRI takes complex values as inputs and denoises to produce a complex-valued 2D image. We computed NMI with 64 bins at each step of the diffusion process to balance complexity with performance. We use the defaults parameters as in ContextMRI, except for the acceleration factor, 16 and the center fraction (ACS), 0.02. We use a pair of anatomy which two contrasts, which has more 30 slices. We consider the slices 15 to 28 as these are more challenging and report the results by using one as the side information for the other.

E Limitations

Our proposed search algorithms lack formal optimality guarantees for exploration–exploitation, and we do not claim they are theoretically optimal. We expect that stronger algorithms are possible, potentially improving both sample efficiency and robustness. A central reason is the absence of a general mathematical framework for designing optimal exploration–exploitation strategies in diffusion-based inverse problems with side information, an open problem we highlight. Practically, this means our methods rely on principled heuristics and tuned schedules (e.g., reward scaling, resampling/branching rates) whose compute allocation is not provably optimal, suggesting a clear direction for future work.

Broader impacts. Our method can improve reconstruction quality in scientific imaging applications such as MRI, with positive impact on diagnostic imaging. Potential negative impacts include increased fidelity of identity-conditioned reconstructions, which raises privacy and consent considerations. In safety-critical domains such as medical imaging, our method should be treated as decision support only, with domain-expert review.

F Use of Large Language Models

Parts of this work were assisted by large language models (specifically GPT-5 from OpenAI). Their use was limited to improving clarity, grammar, and the presentation of experimental descriptions. All conceptual contributions, experimental design, analysis, and final decisions are solely the authors’ responsibility. The models were not used to generate new research ideas, design experiments, or make unverifiable scientific claims. Additionally, large language models were used to generate textual descriptions serving as side information for a specific set of experiments, as detailed in the main paper.